Measurements of intrinsic magnetism in multilayer graphene using cantilever magnetometry

Research Thesis

Presented in partial fulfillment of the requirements for graduation with research distinction in Physics in the undergraduate colleges of The Ohio State University

by

Alex Melendez

The Ohio State University

April 2017

Project Advisors:
P. Chris Hammel, Department of Physics
Ciriyam Jayaprakash, Department of Physics

Abstract

Due to the exponential rate at which technology is progressing, we find ourselves searching for novel nanomaterials at an ever increasing rate as the physical limits of our existing materials are being reached. One such exciting substance is graphene, famous for its extreme electronic characteristics. However one of the many steps necessary in bringing graphene into mainstream technology is the measurement of its intrinsic magnetism. In this thesis we obtain sensitive measurements of the magnetic susceptibility of multilayer graphene using the method of cantilever torque magnetometry, wherein torque exerted on a cantilever is measured from graphene's intrinsic magnetism in the presence of an external field. Fundamental to this process is our development of a method to successfully transfer mesoscopic-sized graphene layers onto micro-mechanical cantilevers. Observations of de Haas-van Alphen oscillations in bulk graphite are obtained, yielding a period of $0.25\,\mathrm{T}^{-1}$. The theoretical physics underlying these phenomena are recapitulated for completeness.

Acknowledgements

I began my affiliation with the Hammel group in Autumn 2015 which was in my third year of undergraduate studies at The Ohio State University. It was at this time that I met the then-graduate student Nicolas Scozzaro, who introduced me to P. Chris Hammel and the rest of the Hammel group. We began to collaborate, and as a year passed we obtained the measurements presented in this thesis. I am deeply grateful to Nic for his mentorship and invested time, as well as to P. Chris Hammel, Simranjeet Singh, Brendan McCullian and others in the Hammel group that have helped me in various ways during my time doing research at OSU.

Contents

List of Figures

Chapter 1

Introduction

Graphene was first theorized to exist in 1947 by P. R. Wallace [1]. Since then, graphene has come to be widely regarded as one of the most promising emergent materials currently known [2]. Unique characteristics such as quasi-relativistic charge carriers and high electrical conductivity cause graphene to be of great interest for fundamental physics as well as engineering applications. In 2004 [3] graphene flakes were shown to be easily and inexpensively producible with simply a piece of graphite and Scotch tape, which allowed for graphene research to become a highly active field and opened the door to the possibility of integrating graphene into modern technology.

A few notable properties of graphene include its high electrical conductivity, thermal conductivity, and electron mobility. Characteristics such as these make graphene highly desirable in a time where our rapidly transforming technology has created a demand for materials with extreme properties. As a result many of the electronic properties of graphene have been extensively studied over the last few decades [4–6], but direct measurements of the intrinsic magnetism remain elusive due to its relatively weak response to applied fields. Despite its asthenic nature, the intrinsic magnetism of graphene must be well understood if graphene is to be optimally integrated with future technologies given the ever decreasing distance between components of electric circuits. The goal of this thesis is to present the measurements made of the intrinsic magnetism of graphene via the technique of cantilever torque magnetometry, as well as a brief review of the theory that establishes the connection between the measured quantity and the magnetism of graphene.

Chapter 2 of this thesis begins with a concise recapitulation of graphene's electrochemical properties, band structure, and intrinsic magnetism. The theory underlying cantilever torque magnetometry is then introduced and an expression for the frequency shift of graphene is obtained. Landau quantization and resulting de Haas-van Alphen effect are derived. Chapter 3 provides the experimental design of the probe and the source of the magnetic field. Chapter 4 details the unique sample preparation process used to transfer graphene and graphite onto cantilevers safely. The results and subsequent discussion provided in Chapter 5 conclude the thesis.

Chapter 2

Theoretical Context

This chapter provides an overview of the physical calculations necessary to understand the significance of the result as well as to become familiar with the mechanism by which the result was related to the directly measured quantity. The calculations begin by describing quantity of interest with respect to the intrinsic magnetism of graphene, which is in this case the magnetic susceptibility. This is then related to the directly measured quantity associated with the experimental apparatus, in this case the cantilever frequency. The sections are ordered in such a way as to make this process appear as straightforward as possible.

Section 2.1 begins by describing of some of the electronic and chemical structure of graphite and graphene as they relate to the electrochemistry of the Carbon atom. General information about the crystal structure and the first Brillouin zone is provided. The real and reciprocal lattice vectors are defined. Section 2.2 provides a basic calculation of the energy density of states assuming the itinerant electrons in graphene are free electrons. In Section 2.3 we obtain the band structure of graphene via the tight binding model as first described in 1947. The effective mass near the Dirac points is calculated and shown to be proportional to the square root of the electronic number density.

Section 2.4, some of the basic physical relations pertaining to electromagnetic fields within materials are briefly reviewed. A general relation between the Zeeman energy and the magnetic susceptibility of a material in the presence of an external magnetic field is obtained.

In Section 2.5, the ball-and-stick model of cantilever torque magnetometry is introduced, and an explicit expression for the Zeeman energy in terms of the susceptibility and field strength is found. The derivation of the dependence of the cantilever frequency on the magnetic susceptibility and field strength is then shown. Section 2.6 goes into more detail about the physical structure of cantilevers, as well as complications arising from linear combinations of modes via the Euler-Bernoulli beam model.

Section 2.7 describes the process of Landau quantization of free electrons and the existence of Landau levels. Landau quantization is the basis of the de Haas-van Alphen effect and other oscillatory behavior in materials. Finally, Section 2.8 provides a derivation of the de Haas-van Alphen effect, the process by which oscillations are observed in the magnetization of a material as a function of the magnetic field.

2.1 Electronic and Crystal Structure of Graphene and Graphite

Carbon is the sixth lightest element, notable for its four valence electrons which are responsible for its incredibly rich chemistry. Indeed, carbon is indisputably the most versatile element when it comes to forming molecules. At the heart of carbon's unique properties lies the electronic structure of carbon.

A lone carbon atom has a ground state electron configuration of $1s^2 2s^2 2p^2$ [7]. When several carbon atoms are condensed into a solid state, the atomic orbitals of each atom may hybridize to form three sp^2 orbitals and one p orbital. The sp^2 orbitals orbitals overlap to form three coplanar σ-bonds at equal angles with a separation of 1.42 Å. The remaining p orbitals are orthogonal to the plane, and overlap to form π-bonds with a p orbital of a neighboring atom. The π-bonds of neighboring pairs hybridize to form bonding and anti-bonding bands, known respectively as π and π^* bands [8]. When many carbon atoms are bonded together in this fashion in a single plane, it creates a two-dimensional hexagonal structure that we call graphene. At standard pressure and temperature these planes stack together under the influence of van der Waals bonds with a separation of 3.35 Å to form graphite.

Graphene can be considered as two interleaving triangular sublattices, denoted by A and B with reference to FIG. 2.1. We can define the primitive lattice vectors of the A triangular lattice as

$$\mathbf{a}_1 = \frac{a}{2}\begin{bmatrix} 3 \\ \sqrt{3} \end{bmatrix} \qquad \text{and} \qquad \mathbf{a}_2 = \frac{a}{2}\begin{bmatrix} 3 \\ -\sqrt{3} \end{bmatrix}. \tag{2.1}$$

The nearest neighbors to an atom in real space are

$$\boldsymbol{\delta}_1 = \frac{a}{2}\begin{bmatrix} 1 \\ \sqrt{3} \end{bmatrix}, \qquad \boldsymbol{\delta}_2 = \frac{a}{2}\begin{bmatrix} 1 \\ -\sqrt{3} \end{bmatrix} \qquad \text{and} \qquad \boldsymbol{\delta}_3 = \begin{bmatrix} -a \\ 0 \end{bmatrix}. \tag{2.2}$$

The next-nearest neighbors can be written in terms of the primitive lattice vectors as

$$\boldsymbol{\delta}'_{\pm 1} = \pm\mathbf{a}_1\,, \qquad \boldsymbol{\delta}'_{\pm 2} = \pm\mathbf{a}_2\,, \qquad \text{and} \qquad \boldsymbol{\delta}'_{\pm 3} = \pm(\mathbf{a}_1 - \mathbf{a}_2)\,. \tag{2.3}$$

The location of the nearest neighbors and next-nearest neighbors will become important in the tight binding model in Section 2.3. Given the primitive lattice vectors $\{\mathbf{a}_1, \mathbf{a}_2\}$, we can find the associated reciprocal lattice vectors $\{\mathbf{b}_1, \mathbf{b}_2\}$ via the relation $\mathbf{a}_i \cdot \mathbf{b}_j = 2\pi\delta_{ij}$. The reciprocal lattice vectors are

$$\mathbf{b}_1 = \frac{2\pi}{3a}\begin{bmatrix} 1 \\ \sqrt{3} \end{bmatrix} \qquad \text{and} \qquad \mathbf{b}_2 = \frac{2\pi}{3a}\begin{bmatrix} 1 \\ -\sqrt{3} \end{bmatrix}. \tag{2.4}$$

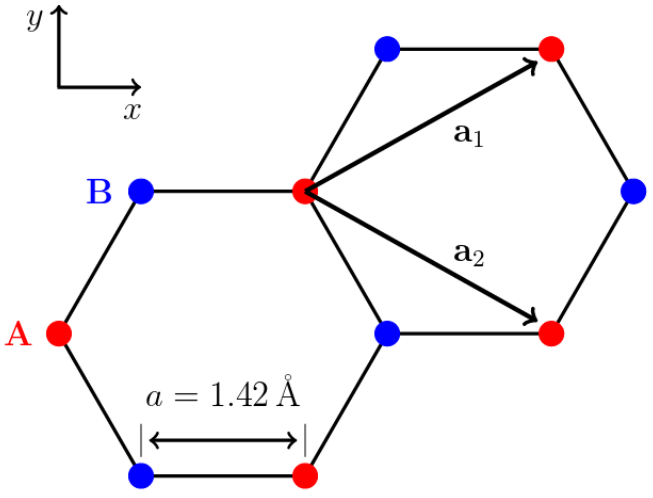

FIGURE 2.1: Ball-and-stick model of graphene crystal structure.

The first Brillouin zone is shown in FIG. 2.2 with the reciprocal lattice vectors. The Brillouin zone has the same hexagonal shape as the real space lattice, but rotated by 90 degrees. The corners of the Brillouin zone labelled by K and K' are known as the Dirac points for each lattice. As we will discuss in Section 2.3, these points are the locations of the Dirac cones in the Fermi surface of graphene according to the tight binding model. These can be written explicitly as vectors in reciprocal space as

$$\mathbf{K} = \frac{2\pi}{3a}\begin{bmatrix} 1 \\ \frac{1}{\sqrt{3}} \end{bmatrix} \qquad \text{and} \qquad \mathbf{K}' = \frac{2\pi}{3a}\begin{bmatrix} 1 \\ -\frac{1}{\sqrt{3}} \end{bmatrix}. \tag{2.5}$$

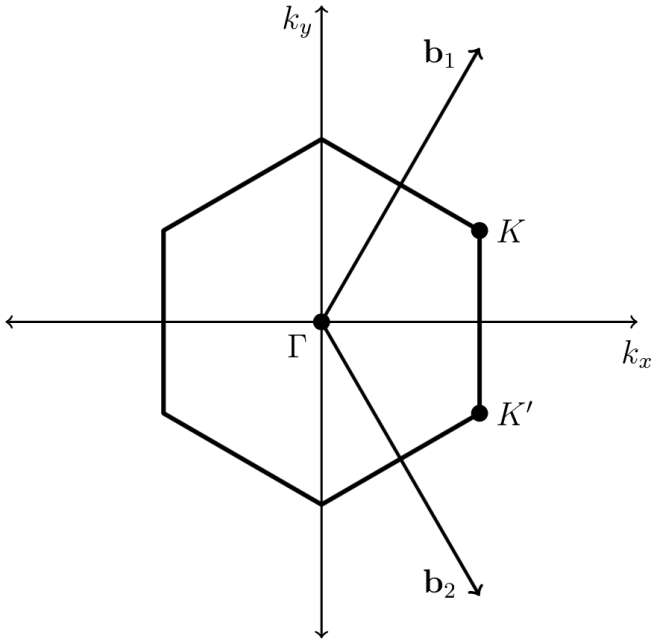

FIGURE 2.2: First Brillouin zone of graphene and reciprocal lattice vectors.

Graphite is a three dimensional crystal that crystallizes in the hexagonal crystal system. Because of this, there are two possible forms of the unit cell: rhombohedral or hexagonal [9]. The former is referred to as beta graphite and the latter as alpha graphite. Beta graphite transforms into alpha graphite when heated over 1300 centigrade. One can reverse the process through mechanical treatment. Typically layers of graphene will not stack directly on top of one another, i.e. they will form rhombohedral cells such that an atom in the first layer will have a nearest neighbor in the second layer that is above the center of the hexagons in the first layer. However there are three unique ways that the layers can stack, and this allows different arrangements such as rhombohedral stacking ($123123\cdots$) and Bernal stacking ($1212\cdots$). A single piece of bulk graphite may

contain many different stacking orders. One can use the tight binding model to arrive at an analytical expression for the band structure of bulk graphite, provided that there is perfect Bernal stacking. Graphite is relatively highly anisotropic in many respects due to its crystal structure. Its electrical conductivity and phonon propagation speed vary dramatically based on their respective angles as measured from the plane of the graphene, e.g. graphite is highly electrically conductive parallel to the planes and poorly conductive perpendicular to the planes.

2.2 Density of States of Graphene as a Free Electron Gas

To obtain a first estimate for the density of states of graphene, we can assume the system to be a free electron gas where each atom contributes one itinerant electron. Each state can be occupied by two electrons due to spin degeneracy, so the band is exactly half-filled. Graphene can therefore be considered to be a perfect semi-metal. As a result the itinerant electrons in graphene are highly mobile, so the free electron approximation is relatively reasonable despite the fact that in the following section we will obtain the band structure via the tight binding model.

The free electron model of metals is a generalization of the Drude theory of metals in order to account for the Fermi statistics of electrons [10, 11]. In free electron (also known as Sommerfeld) theory, itinerant electrons in a two-dimensional metal are modeled as a free electron gas of area $A = L^2$, occupied according to the Fermi factor

$$n_F\big[\beta(E(\mathbf{k}) - \mu)\big] = \frac{1}{e^{\beta(E(\mathbf{k})-\mu)} + 1}\,. \tag{2.6}$$

It follows then that the total number of electrons is given by

$$N = g_s \sum_{\mathbf{k}} n_F\big[\beta(E(\mathbf{k}) - \mu)\big]\,, \tag{2.7}$$

where $g_s = 2$ accounts for spin degeneracy. The wavefunctions for free electrons are of the form $\psi_{\mathbf{k}}(\mathbf{r}) \propto e^{i\mathbf{k}\cdot\mathbf{r}}$. Using periodic (i.e. $e^{ikr} = e^{ik(r+L)}$) boundary conditions, the values of the wavevector are quantized to

$$\mathbf{k} = \frac{2\pi}{L}\begin{bmatrix} n_1 \\ n_2 \end{bmatrix} \qquad \text{for } n_1,\, n_2 \in \mathbb{N}\,. \tag{2.8}$$

For large L, Eq. (2.7) can be written as the following integral:

$$N = g_s \left(\frac{L}{2\pi}\right)^2 \int n_F\big[\beta(E(\mathbf{k}) - \mu)\big]\,\mathrm{d}\mathbf{k}\,. \tag{2.9}$$

In the zero temperature limit, the Fermi occupation factor in Eq. (2.9) becomes the Heaviside function

$$\lim_{T\to 0} n_F\big[\beta(E(\mathbf{k}) - \mu)\big] = \Theta\big(E_F - E(\mathbf{k})\big)\,, \tag{2.10}$$

where the Fermi energy E_F is defined as the value of the chemical potential at zero temperature. The total electron number now reduces to an integral over a circular area:

$$N = g_s \frac{A}{4\pi^2} \int^{|k|<k_F} \mathrm{d}\mathbf{k} = g_s \frac{A}{4\pi^2} \int_0^{2\pi} \int_0^{k_F} k \, \mathrm{d}k \, \mathrm{d}\phi = g_s \frac{Ak_F^2}{4\pi} \,. \tag{2.11}$$

The areal density of the electrons is therefore

$$n_A = \frac{N}{A} = g_s \frac{k_F^2}{4\pi} = g_s \frac{mE_F}{2\pi\hbar^2} \,. \tag{2.12}$$

It then follows that the energy density of the states per unit area (including spin degeneracy) at zero temperature is

$$g(E) = \frac{\mathrm{d}n}{\mathrm{d}E} = \frac{g_s m}{2\pi\hbar^2} = \frac{m}{\pi\hbar^2} \,. \tag{2.13}$$

A major shortcoming of applying the free electron model to graphene is that it does not take into account the interaction between electrons and the crystal lattice, and as such it fails to predict the correct band structure. However one can do a better job through the use of the nearly free elecron model. The nearly free electron model was developed as a modification to the free electron model through the use of perturbation theory. The nearly free electron model is a correction to the free electron model wherein the crystal lattice is regarded as providing a weak (i.e. perturbing) periodic potential energy with the same periodicity as the lattice. The associated wavefunctions are of the Bloch form $\psi_{\mathbf{k}}(\mathbf{r}) = u_{\mathbf{k}}(\mathbf{r})e^{i\mathbf{k}\cdot\mathbf{r}}$, where $u_{\mathbf{k}}(\mathbf{r})$ must also periodic with the lattice [10, 11].

The nearly free electron model considers electron to be essentially free to move within the entirety of the crystal with only a weak interaction with their respective ions in the lattice. There exist alternative approaches to calculating the electronic properties of graphene viewed from the opposite extreme, i.e. the electrons can be considered to be bound strongly to their respective atoms and only weakly interact with the surrounding lattice. In the next section we will discuss an approach such as this known as the tight binding model.

2.3 Tight Binding Model of Graphene Band Structure

The tight binding model is a variational approach in which electrons are considered to be tightly bound to their respective nuclei, but can "hop" to an arbitrary number of neighboring atoms in the lattice [10, 11]. The tight binding model allows one to approximate the exact wavefunction with a linear combination of known atomic orbitals. The ions nearest to a given electron have the largest effect on its energy, so the result will be close to the ionization energy of the electron. This model was first used to calculate the band structure of graphene in 1947 [1]. The tight binding description was later generalized to incorporate infinitely many layers of graphene (i.e. bulk graphite) and is known as the Slonczewski-Weiss-McClure model [12].

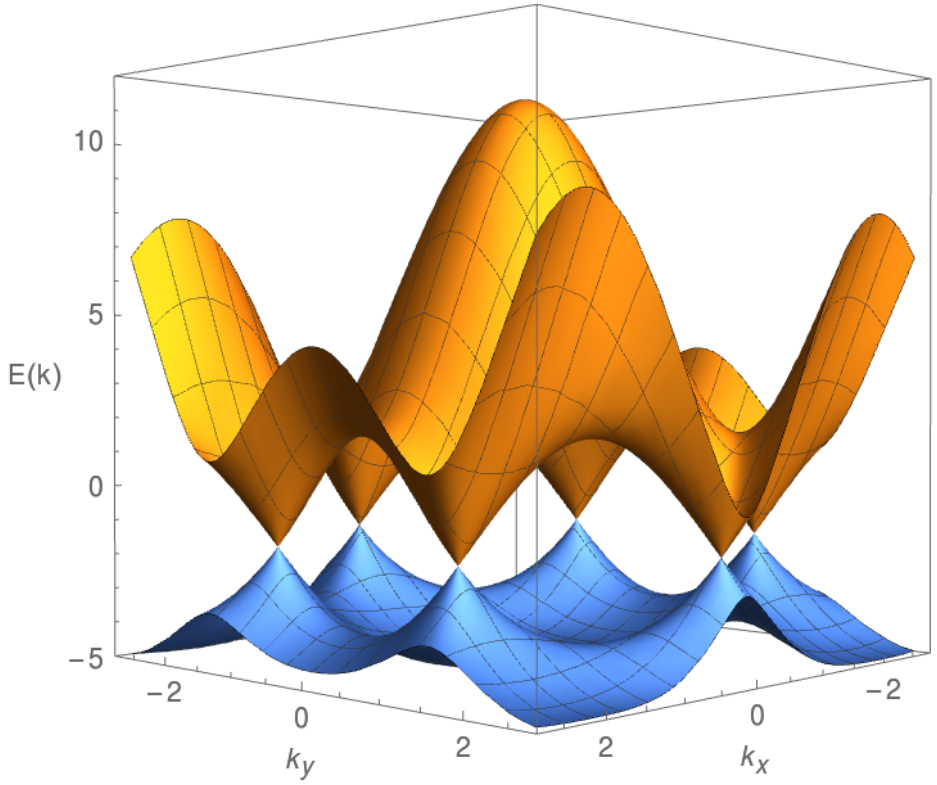

FIGURE 2.3: Fermi surface pertaining to one hexagon of graphene in reciprocal space, where k_x and k_y are plotted in units of $1/a$, and $E(\mathbf{k})$ is plotted in eV.

Considering only hopping between nearest-neighbors and next-nearest-neighbors, the second quantization Hamiltonian is given by

$$\mathcal{H}_{\text{TB}} = -t \sum_{\langle i,j\rangle,\boldsymbol{\sigma}} \left(a^{\dagger}_{\boldsymbol{\sigma},i} b_{\boldsymbol{\sigma},j} + \text{h.c.} \right) - t' \sum_{\langle\langle i,j\rangle\rangle,\boldsymbol{\sigma}} \left(a^{\dagger}_{\boldsymbol{\sigma},i} a_{\boldsymbol{\sigma},j} + b^{\dagger}_{\boldsymbol{\sigma},i} b_{\boldsymbol{\sigma},j} + \text{h.c.} \right), \tag{2.14}$$

where $a_{\boldsymbol{\sigma},i}$ and $b_{\boldsymbol{\sigma},i}$ are electron annihilation operators for lattices A and B respectively. In Eq. (2.14) we have used units such that $\hbar = 1$. It can be shown that the dispersion relation for graphene is given by [1]

$$E_+(\mathbf{k}) = +t\sqrt{3 + f(\mathbf{k})} - t' f(\mathbf{k}) \tag{2.15}$$

$$E_-(\mathbf{k}) = -t\sqrt{3 + f(\mathbf{k})} - t' f(\mathbf{k}), \tag{2.16}$$

where

$$f(\mathbf{k}) = 2\cos\left(\sqrt{3} k_y a\right) + 4\cos\left(\frac{\sqrt{3}}{2} k_y a\right) \cos\left(\frac{3}{2} k_x a\right). \tag{2.17}$$

with $t = 2.7\,\text{eV}$ and $t' = -0.2t$. The Fermi surface of graphene is shown in FIG. 2.3. The band described by $E_+(\mathbf{k})$ is the π^*-band, and the band described by $E_-(\mathbf{k})$ is the π-band. At each K and K' point, the two bands touch at a single point at which they take on a conical shape. These cones are called Dirac cones, and they are points where the dispersion relation is approximately linear. When Eq. (2.15) and (2.16) are expanded around the Dirac points, one obtains

$$E_+(\mathbf{q}) \approx +\hbar v_F |\mathbf{q}| + \mathcal{O}\big((q/K)^2\big) \tag{2.18}$$

$$E_-(\mathbf{q}) \approx -\hbar v_F |\mathbf{q}| + \mathcal{O}\big((q/K)^2\big), \tag{2.19}$$

where $\mathbf{q} \equiv \mathbf{k} - \mathbf{K}$ (or $\mathbf{K}'$). If we include t' to second order in (q/K), then we can write

$$E_+(\mathbf{q}) \approx 3t' + \hbar v_F |\mathbf{q}| - \left(\frac{9t'a^2}{4} + \frac{3ta^2}{8} \sin\left(3\theta_{\mathbf{q}}\right) \right) |\mathbf{q}|^2 \tag{2.20}$$

$$E_-(\mathbf{q}) \approx 3t' - \hbar v_F |\mathbf{q}| - \left(\frac{9t'a^2}{4} - \frac{3ta^2}{8} \sin\left(3\theta_{\mathbf{q}}\right) \right) |\mathbf{q}|^2, \tag{2.21}$$

where

$$\theta_{\mathbf{q}} \equiv \tan^{-1}\left(\frac{q_x}{q_y}\right). \tag{2.22}$$

The linear dispersion relation is characteristic of relativistic particles, analogous to those described by the Dirac equation for massless particles. For this reason the K and K' points are known as Dirac points. As such, electrons with a $\mathbf{k}$ near the Dirac points in reciprocal space exhibit relativistic behavior. The associated cyclotron mass is defined as [8]

$$m_c^* = \frac{\hbar^2}{2\pi} \frac{\partial S(E)}{\partial E}\bigg|_{E=E_F} , \tag{2.23}$$

where $S(E) = \pi|\mathbf{q}(E)|^2$ is the area in reciprocal space enclosed by the orbit in the semi-classical approximation. In this case we have

$$S(E) = \pi q^2 = \frac{\pi E^2}{\hbar^2 v_F^2} . \tag{2.24}$$

Given $E_F = \hbar v_F k_F$, then this yields

$$m_c^* = \frac{E_F}{v_F^2} = \frac{\hbar k_F}{v_F} . \tag{2.25}$$

We found in Eq. (2.12) that the electron number density was given by $n_A = k_F^2/2\pi$. Adding an extra factor of two to account for valley degeneracy, the new electron density is

$$n_A = \frac{k_F^2}{\pi} . \tag{2.26}$$

The Fermi wavevector is then $k_F = \sqrt{\pi n_A}$, which allows Eq. (2.25) to be written as [8]

$$m_c^* = \frac{\hbar}{v_F}\sqrt{\pi n_A} , \tag{2.27}$$

where for graphene $v_F \approx 10^6$ m/s is the Fermi velocity and $n_A = 10^{17}/\mathrm{m}^2$ is the particle number density. The cyclotron mass therefore depends on the square root of the electronic number density. Note that the effective cyclotron mass is equal to the effective mass at the Fermi level m_F^*.

2.4 Intrinsic Magnetism of Graphene in an External Field

In this section we are interested in the relationship between the magnetic susceptibility of graphene and the associated Zeeman energy when an external field is applied to graphene. The dependence of the Zeeman energy on the susceptibility is the crucial factor that makes cantilever magnetometry possible with weak diamagnetic materials such as thin graphite and graphene. Here we will take a classical approach, in which we consider graphene to be a homogeneous two dimensional material where the magnetic susceptibility in the x and y directions in the plane are considered to be equal, that is $\chi_x = \chi_y = \chi_\parallel$. For simplicity we work in the frame of reference of graphene in this section. In Section 2.5 we obtain an explicit expression for the energy in terms of the applied field as measured in the laboratory frame.

Within a material, the total field $\mathbf{B}$ is a sum of the externally applied field $\mathbf{B}_0 = \mu_0\mathbf{H}$ and the induced intensity of magnetization $\mathbf{I} = \mu_0\mathbf{M}$, where μ_0 is the vacuum permeability and $\mathbf{H}$ is the field strength [13, 14]. The relationship between magnetization $\mathbf{M}$ of a material and the field strength is quantified by the volume magnetic susceptibility tensor $\hat{\chi}$, defined by

$$\mathbf{M} = \hat{\chi}\mathbf{H}\,. \tag{2.28}$$

This allows the total field to be written in terms of the magnetic susceptibility as shown in Eq. (2.29).

$$\mathbf{B} = \mathbf{B}_0 + \mathbf{I} = \mu_0\left(1 + \hat{\chi}\right)\mathbf{H}\,. \tag{2.29}$$

For a sample of uniform density, the magnetic moment is related to the magnetization by the relation

$$\mathbf{m} = V\mathbf{M}\,. \tag{2.30}$$

where V is the volume of the sample. In the presence of an external magnetic field, a magnetic moment $\mathbf{m}$ experiences the torque $\boldsymbol{\tau} = \mathbf{m} \times \mathbf{B}$, where $\mathbf{B}$ denotes the total field. The potential energy associated with this torque is known as the Zeeman energy,

defined as [13, 14]

$$U_{\text{Zeeman}} = -\mathbf{m} \cdot \mathbf{B}\,. \tag{2.31}$$

Plugging in equations (2.29) and (2.30), the Zeeman energy can be written as a function of the field strength and susceptibility:

$$\begin{aligned} U_{\text{Zeeman}} &= -\left(V\mathbf{M}\right) \cdot \mu_0 \left(1 + \hat{\chi}\right) \mathbf{H} && (2.32)\\ &= -\mu_0 V \hat{\chi}\mathbf{H} \cdot \left(\mathbf{H} + \hat{\chi}\mathbf{H}\right) && (2.33)\\ U_{\text{Zeeman}} &= -\mu_0 V \Big[\left(\hat{\chi}\mathbf{H}\right) \cdot \mathbf{H} + |\hat{\chi}\mathbf{H}|^2 \Big]\,. && (2.34) \end{aligned}$$

Considering the basis of graphene to be two dimensional (i.e. in-plane or out of plane), then working in this basis the magnetic susceptibility takes the form of a diagonal matrix as shown in Eq. (2.35). For clarification, the notation $[\,\cdot\,]_{\text{basis}}$ is used here to denote the basis in which an element is expressed.

$$\left[\hat{\chi}\right]_{\perp\text{-}\parallel} = \begin{bmatrix} \chi_\perp & 0 \\ 0 & \chi_\parallel \end{bmatrix}_{\perp\text{-}\parallel}\,. \tag{2.35}$$

In this case, the magnetic moment is given in terms of the magnetic field strength and the susceptibility in the $\perp$ - $\parallel$ basis as

$$\left[\mathbf{m}\right]_{\perp\text{-}\parallel} = V\left[\mathbf{M}\right]_{\perp\text{-}\parallel} = V\left[\hat{\chi}\mathbf{H}\right]_{\perp\text{-}\parallel} = V \begin{bmatrix} \chi_\perp H_\perp \\ \chi_\parallel H_\parallel \end{bmatrix}_{\perp\text{-}\parallel}\,. \tag{2.36}$$

The total field in this basis is therefore

$$\left[\mathbf{B}\right]_{\perp\text{-}\parallel} = \hat{\mu}\left[\mathbf{H}\right]_{\perp\text{-}\parallel} = \mu_0 \left(1 + \hat{\chi}\right) \left[\mathbf{H}\right]_{\perp\text{-}\parallel} = \mu_0 \begin{bmatrix} \left(1 + \chi_\perp\right) H_\perp \\ \left(1 + \chi_\parallel\right) H_\parallel \end{bmatrix}_{\perp\text{-}\parallel}\,. \tag{2.37}$$

In terms of the still unknown $H_\perp$ and $H_\parallel$, we can write the Zeeman energy as

$$U_{\text{Zeeman}} = -\mu_0 V \left[\chi_\perp(1+\chi_\perp)H_\perp^2 + \chi_\parallel(1+\chi_\parallel)H_\parallel^2\right]. \tag{2.38}$$

2.5 Cantilever Torque Magnetometry

In this section we discuss the physics behind the experimental technique of cantilever torque magnetometry, the method by which the data presented in this thesis was obtained. The fundamental goal of cantilever magnetometry is to obtain information about the magnetic moment of a material with excellent sensitivity, typically able to measure a moment as weak as 10^{-15} J/T [15]. However it has been shown that, in principle, cantilever magnetometry can detect moments on the order of 10^{-19} J/T [16]. Other methods have been developed in the past to sensitively measure magnetic moments such as SQUID magnetometry, but lack the requisite sensitivity with a minimum of about 10^{-12} J/T. Cantilevers behave as classical resonant systems with a fundamental resonant frequency and quantized higher order modes, similar to strings under tension. More will be said about the higher harmonics of cantilevers in Section 2.6, but here we will only consider the cantilever oscillating in its ground state. Typical cantilevers used for this purpose are made of thin silicon with a length of 100-400 μm. In our experiments we used two types of cantilevers, larger triangle cantilevers as shown in Fig. 4.4 and smaller ultra-soft cantilevers as shown in Fig. 4.5.

The basic idea of cantilever torque magnetometry is as follows. Under a vacuum, undriven cantilevers will naturally oscillate at their resonant frequencies due to random thermal excitations. The desired sample is first adhered to the tip of a cantilever (this is a nontrivial step in the process of sample preparation as will be discussed further in Section 4). The cantilever is put inside of a solenoid capable of high magnetic fields and under a high vacuum. When the magnetic field is turned on the sample will magnetize. This will cause an associated torque on the sample given that $\boldsymbol{\tau} = \mathbf{m} \times \mathbf{B}$ [13, 14]. Given that the sample is adhered to the cantilever, this manifests as an effective torque on the cantilever. As we shall show in the equations below, this torque will cause a frequency shift can be measured. In Section 3 we detail the process by which this frequency was measured. The frequency shift can be positive or negative depending on the relative orientations of the cantilever's equilibrium position and the applied field.

In the previous section we calculated the Zeeman energy associated with graphene in terms of the components of the applied field $H_\perp$ and $H_\parallel$ in the directions perpendicular and parallel to the plane respectively. However these components are constantly changing values as the plane of the graphene changes orientation with respect to the

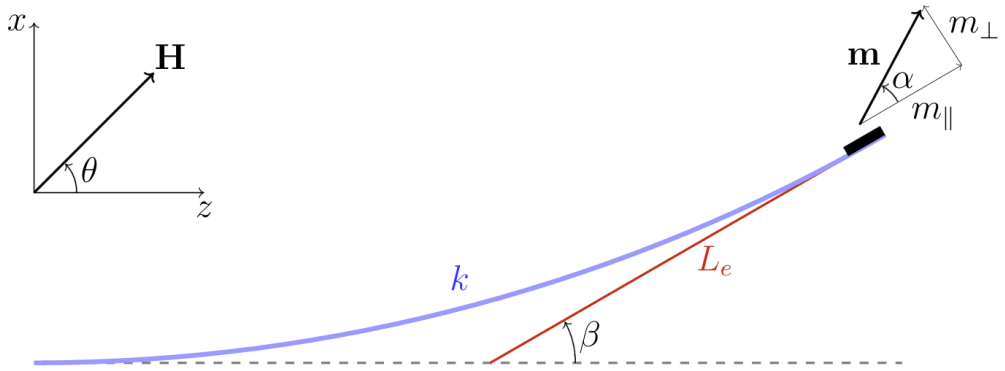

FIGURE 2.4: Model of Cantilever with Magnetic Sample.

field due to the oscillations of the cantilever, and also depend on the orientation of the external field with respect to the cantilever's equilibrium position. As such, we must now consider the specifics of the cantilever's motion to determine the relationship between the magnetic susceptibility and the frequency shift as a function of the field.

With reference to FIG. 2.4, the magnetic field strength can be written in the x-z basis as

$$[\mathbf{H}]_{x\text{-}z} = \begin{bmatrix} H_x \\ H_z \end{bmatrix}_{x\text{-}z} = \begin{bmatrix} H\sin\theta \\ H\cos\theta \end{bmatrix}_{x\text{-}z} . \tag{2.39}$$

To must consider a time-dependent linear transformation in order to express $\mathbf{H}$ in the $\perp$ - $\parallel$ basis. The rotation matrix $\mathcal{R}_\beta$ associated with this transformation is

$$\mathcal{R}_\beta = \begin{bmatrix} \cos\beta & -\sin\beta \\ \sin\beta & \cos\beta \end{bmatrix} . \tag{2.40}$$

where β is the angle of the cantilever (i.e. the graphene) with respect to its angle at equilibrium and as such is a function of time. The magnetic field strength in the $\perp$ - $\parallel$ basis is therefore

$$[\mathbf{H}]_{\perp\text{-}\parallel} = \begin{bmatrix} H_\perp \\ H_\parallel \end{bmatrix}_{\perp\text{-}\parallel} = \mathcal{R}_\beta [\mathbf{H}]_{x\text{-}z} = \begin{bmatrix} H\sin(\theta-\beta) \\ H\cos(\theta-\beta) \end{bmatrix}_{\perp\text{-}\parallel} . \tag{2.41}$$

Given Eq. (2.41) we are finally able to calculate the Zeeman energy explicitly. Evaluating Eq. (2.38) yields the result [17]

$$U_{\text{Zeeman}} = -\mu_0 V H^2 \left[\chi_\perp(1+\chi_\perp)\sin^2(\theta-\beta) + \chi_\parallel(1+\chi_\parallel)\cos^2(\theta-\beta)\right] . \tag{2.42}$$

Here we will assume the oscillations of the cantilever constitute only small deviations about the equilibrium, i.e. $\beta \approx 0$. As a result, the system can be modeled as a simple harmonic oscillator with effective length L_e, as illustrated in FIG. 2.4. The effective length is chosen such that its associated geometric line is tangent to the sample, which is constant to first order when $\beta \approx 0$. The system therefore has the associated spring potential energy $U_{\text{spring}} = \frac{1}{2}k(L_e\beta)^2$, where k is the spring constant. The classical Lagrangian for such a system is

$$\mathcal{L} = T - U_{\text{spring}} - U_{\text{Zeeman}} . \tag{2.43}$$

In this case the Lagrangian takes the form [18]

$$\mathcal{L} = \tfrac{1}{2}mL_e^2\dot{\beta}^2 - \tfrac{1}{2}kL_e^2\beta^2 + \mathbf{m}\cdot\mathbf{B} . \tag{2.44}$$

In order to obtain an expression for the cantilever frequency as a function of the susceptibility, we must consider the Euler-Lagrange equation

$$\frac{\mathrm{d}}{\mathrm{d}t}\frac{\partial\mathcal{L}}{\partial\dot{\beta}} = \frac{\partial\mathcal{L}}{\partial\beta} . \tag{2.45}$$

For convenience here we can make the definition

$$\chi_\Delta \equiv \chi_\parallel(1+\chi_\parallel) - \chi_\perp(1+\chi_\perp) . \tag{2.46}$$

Evaluating the Euler-Lagrange equation in Eq. (2.45) to reduces to

$$mL_e^2\ddot{\beta} = -kL_e^2\beta + 2\mu_0 V H^2 \sin(\theta-\beta)\cos(\theta-\beta)\chi_\Delta . \tag{2.47}$$

When $\beta \approx 0$, we can make the approximation $\sin(\theta-\beta)\cos(\theta-\beta) \approx \frac{1}{2}\sin(2\theta) - \beta\cos(2\theta)$. Rearranging then yields

$$\ddot{\beta} + \left(1 + \frac{2\mu_0 V H^2 \cos(2\theta)}{kL_e^2}\chi_\Delta\right)\omega_0^2\beta + C = 0\,, \tag{2.48}$$

for some C independent of β. We need not evaluate this equation further, since it is of the form

$$\ddot{\beta} + \omega^2\beta + C = 0\,. \tag{2.49}$$

Dimensional analysis then implies that the new frequency is given by

$$\omega = \omega_0\sqrt{1 + \frac{2\mu_0 V H^2 \cos(2\theta)}{kL_e^2}\chi_\Delta}\,. \tag{2.50}$$

The rightmost term in the radical is small relative to unity, which allows us to make the binomial approximation $\sqrt{1+\epsilon} \approx 1 + \frac{1}{2}\epsilon$ for $\epsilon \approx 0$. Hence the frequency is approximately

$$\omega \approx \omega_0\left(1 + \frac{\mu_0 V H^2 \cos(2\theta)}{kL_e^2}\chi_\Delta\right)\,. \tag{2.51}$$

Recalling that $B_0 = \mu_0 H$, frequency can be written as

$$\omega \approx \omega_0\left(1 + \frac{V B^2 \cos(2\theta)}{\mu_0 kL_e^2}\chi_\Delta\right)\,. \tag{2.52}$$

The frequency shift of the cantilever as a function of the magnetic susceptibility and the external field is therefore [17]

$$\frac{\Delta\omega}{\omega_0} = \frac{V B_0^2 \cos(2\theta)}{\mu_0 kL_e^2}\chi_\Delta\,, \tag{2.53}$$

where again $\chi_\Delta \equiv \chi_\parallel(1+\chi_\parallel) - \chi_\perp(1+\chi_\perp)$. Given a method to measure the frequency shift of the cantilever, one can calculate the quantity $V\chi_\Delta$. Typically the volume is easily estimated since the surface area of the sample is clearly visible and the thickness can be estimated to within a few layers for thin graphene stacks, so in principle one can isolate factor χ_Δ. The component of the susceptibilities of graphite have been measured to be small, with an out-of-plane susceptibility for bulk HOPG of $\chi_\perp \approx -6\times10^{-4}$ at 300 K and an even smaller in-plane susceptibility of $\chi_\parallel \approx -1\times10^{-5}$ [19]. This allows us

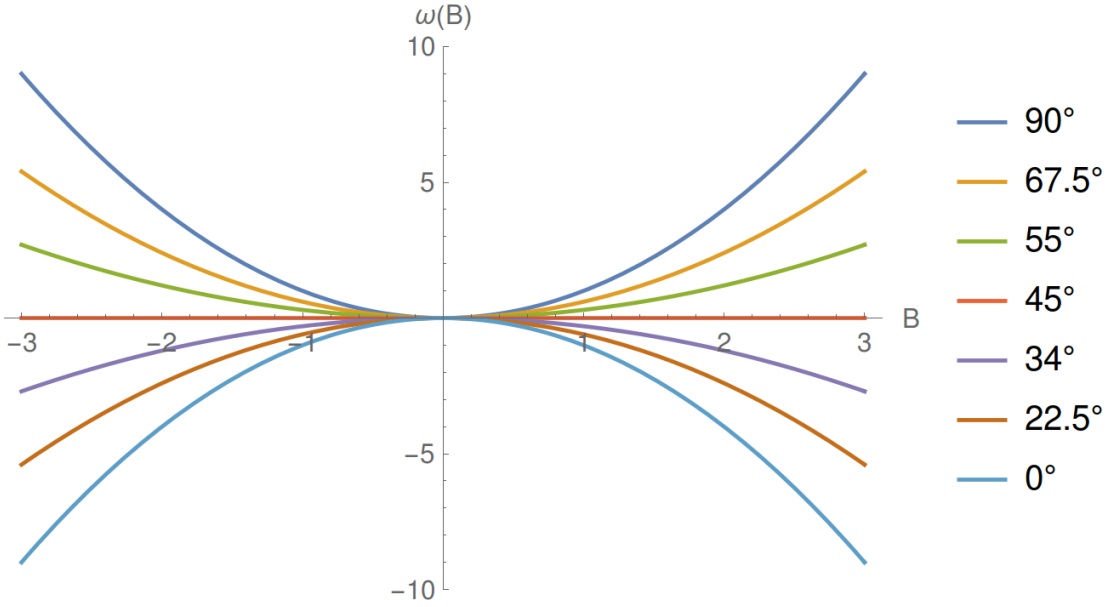

FIGURE 2.5: Predicted frequency shift of cantilever as a function of the field plotted with unitless variables, exhibiting dependence of the frequency shift on the magnitude of the external field squared and the angle of the magnetic field as $\cos(2\theta)$.

to approximate $\chi_\Delta \approx \chi_\perp$, allowing us to write the final equation for the frequency as

$$\frac{\Delta\omega}{\omega_0} = \frac{VB_0^2\cos(2\theta)}{\mu_0 k L_e^2}\chi_\perp \,. \tag{2.54}$$

The frequency therefore has a parabolic frequency shift as a function of the applied field and depends on the out-of-plane susceptibility linearly. The $\cos(2\theta)$ factor reflects the symmetry of the system. In this derivation we have made several approximations, but as we will show in Section 5, the theory fits the data reasonably well.

2.6 Cantilevers as Euler-Bernoulli Beams

In this section we will briefly consider a more rigorous approach to cantilever motion. We will not derive any physics directly relevant to the results in this thesis, but the information in this section should be noted given that cantilevers can occasionally oscillate in modes other than the lowest order mode or a superposition of modes. As such one should take care to use a clean, unbent cantilever for all measurements. In order to understand the nature of this behavior to some degree, we can consider a cantilever in the context of Euler-Bernoulli beam theory.

The cantilever can be modeled as an Euler-Bernoulli beam that experiences deflection when subject to an applied load, given by the static equation [20]

$$\frac{\mathrm{d}^2}{\mathrm{d}z^2}\left(EI\frac{\mathrm{d}^2x}{\mathrm{d}z^2}\right) = q(z)\,. \tag{2.55}$$

Here the product EI is known as the flexural rigidity, where E is the elastic modulus and I is the moment of inertia. Using the same coordinates as in FIG. 2.4, the amplitude of the cantilever with respect to the equilibrium position is given by $x(z)$ and the distributed load is $q(z)$. The Euler-Lagrange equation for a dynamic Euler-Bernoulli beam is

$$\frac{\partial^2}{\partial z^2}\left(EI\frac{\partial^2x}{\partial z^2}\right) = -\rho\frac{\partial^2x}{\partial t^2} + q(z)\,. \tag{2.56}$$

Assuming a uniform density, a constant flexural rigidity and a zero distributed load, then the method of separation of variables yields the following ordinary differential equation for the position:

$$\frac{\mathrm{d}^4x(z)}{\mathrm{d}z^4} = \beta^4x(z)\,, \tag{2.57}$$

where $\beta^4 \equiv \omega^2 m/EI$ for mass $m = \rho A(z)$ and circular natural frequency ω. The solutions to Eq. (2.56) are hyperbolic curves of the form

$$x_n(z) = A_n\cos(\beta_n z) + B_n\sin(\beta_n z) + C_n\cosh(\beta_n z) + D_n\sinh(\beta_n z)\,. \tag{2.58}$$

The boundary conditions associated with a cantilevered beam of length L are

$$\begin{cases} x(0) = 0 \\ x'(0) = 0 \end{cases} \text{(fixed end)} \qquad \text{and} \qquad \begin{cases} x''(L) = 0 \\ x^{(3)}(L) = 0 \end{cases} \text{(free end).} \tag{2.59}$$

Imposing the boundary conditions in Eq. (2.58), one obtains

$$x_n(z) = A_n \left(\left[\cosh(\beta_n z) - \cos(\beta_n z) \right] + \frac{\cos(\beta_n L) + \cosh(\beta_n L)}{\sin(\beta_n L) + \sinh(\beta_n L)} \left[\sin(\beta_n z) - \sinh(\beta_n z) \right] \right) . \tag{2.60}$$

The lowest three modes of the cantilever given by Eq. (2.60) have been plotted in FIG. 2.6.

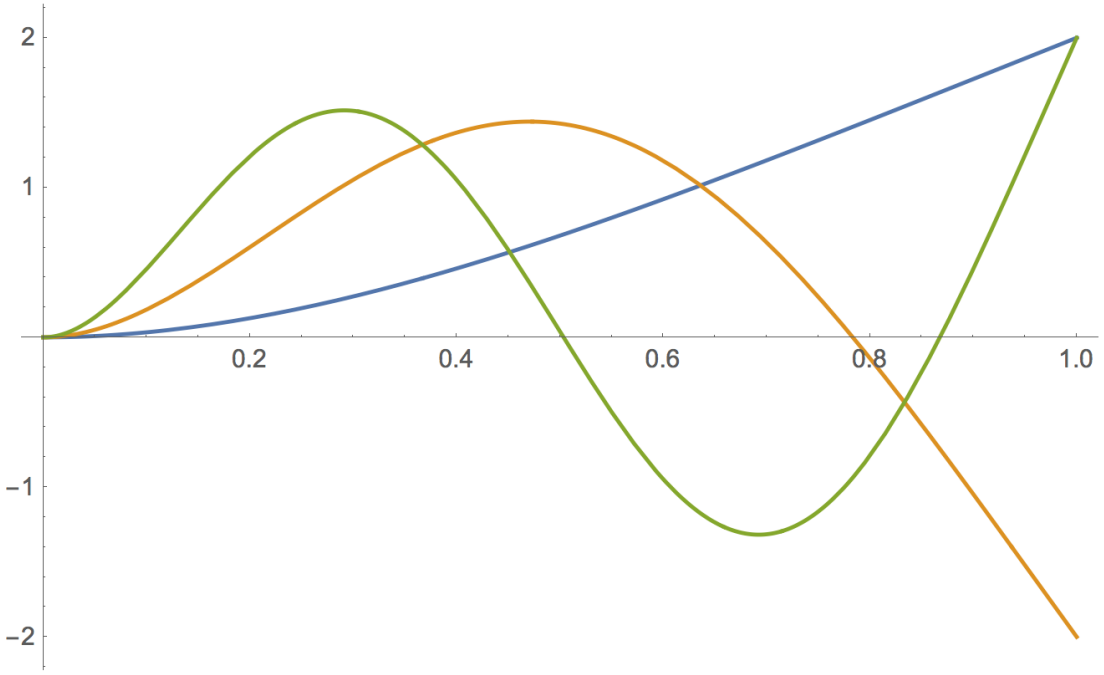

FIGURE 2.6: The first three (unnormalized) modes of a dynamic Euler-Bernoulli beam plotted with unitless parameters.

2.7 Landau Quantization of Free Electrons

In this section we provide a brief review of the phenomenon of Landau quantization of free electrons, available in most graduate solid state textbooks. Analogous to classically charged particles, electrons will exhibit cyclotron motion in the presence of an external field. However since the electrons are quantum mechanical, they can only occupy quantized cyclotron orbits with associated quantized energies known as Landau levels. Landau quantization is responsible for such phenomena as the Shubnikov-de Haas effect and the de Haas-van Alphen effect as will be discussed in Section 2.8. It is for this reason that the derivation is reiterated here.

Consider an electron moving with velocity $\mathbf{v}$ in the presence of an external field $\mathbf{B}$. The canonical momentum is [13, 14]

$$\mathbf{p} = \mathbf{p}_{\text{kinematic}} + \mathbf{p}_{\text{field}}\,, \tag{2.61}$$

where $\mathbf{p}_{\text{kinematic}} = \hbar\mathbf{k}$ is the familiar kinematic momentum and $\mathbf{p}_{\text{field}}$ is the field momentum associated with a charged particle moving through an electromagnetic field. The field momentum in this case is given by

$$\mathbf{p}_{\text{field}} = \frac{1}{4\pi}\int \mathbf{E}\times\mathbf{B}\,\mathrm{d}V = -e\mathbf{A}\,, \tag{2.62}$$

where we have assumed that the electrons are moving through a non-magnetic material such that $\mathbf{B} = \mathbf{H}$. Here $\mathbf{A}$ is the vector potential, defined in relation to a magnetic field as $\mathbf{B} = \boldsymbol{\nabla}\times\mathbf{A}$. The canonical momentum is therefore $\mathbf{p} = \hbar\mathbf{k} - e\mathbf{A}$. The Hamiltonian for the system can then be written as

$$\mathcal{H} = \frac{1}{2m_e}\mathbf{p}^2 = \frac{1}{2m_e}\left(\hbar\mathbf{k} + e\mathbf{A}\right)^2. \tag{2.63}$$

The equation of motion for the electron moving through $\mathbf{B}$ is

$$\frac{\mathrm{d}\mathbf{p}}{\mathrm{d}t} = \mathbf{F}_{\text{Lorentz}} \qquad \Longrightarrow \qquad \hbar\frac{\mathrm{d}\mathbf{k}}{\mathrm{d}t} = -e\,\mathbf{v}\times\mathbf{B}\,. \tag{2.64}$$

Integration with respect to time yields

$$\mathbf{p}_{\text{kinematic}} = \hbar\mathbf{k} = -e\,\mathbf{r}\times\mathbf{B}\,. \tag{2.65}$$

The cyclotron orbit of the electron is quantized according to the Bohr-Sommerfeld relation [11]

$$\oint \mathbf{p} \cdot \mathrm{d}\mathbf{r} = 2\pi\hbar \left(n + \frac{1}{2}\right), \tag{2.66}$$

where $n = 0, 1, 2, \cdots$. We can write the integral in Eq. (2.66) in terms of the magnetic flux $\Phi = \mathbf{B} \cdot \boldsymbol{\mathcal{A}}$ as

$$\begin{aligned}
\oint \mathbf{p} \cdot \mathrm{d}\mathbf{r} &= \hbar \oint \mathbf{k} \cdot \mathrm{d}\mathbf{r} - e \oint \mathbf{A} \cdot \mathrm{d}\mathbf{r} && (2.67)\\
&= -e \oint \mathbf{r} \times \mathbf{B} \cdot \mathrm{d}\mathbf{r} - e \int \boldsymbol{\nabla} \times \mathbf{A} \cdot \mathrm{d}\boldsymbol{\sigma} && (2.68)\\
&= e\,\mathbf{B} \cdot \oint \mathbf{r} \times \mathrm{d}\mathbf{r} - e \int \mathbf{B} \cdot \mathrm{d}\boldsymbol{\sigma} && (2.69)\\
&= 2e\,\mathbf{B} \cdot \boldsymbol{\mathcal{A}} - e\,\mathbf{B} \cdot \boldsymbol{\mathcal{A}} && (2.70)\\
\oint \mathbf{p} \cdot \mathrm{d}\mathbf{r} &= e\Phi\,. && (2.71)
\end{aligned}$$

Equation (2.68) was obtained using Stokes' theorem, and Eq. (2.70) was obtained using the fact that $2\boldsymbol{\mathcal{A}} = \oint \mathbf{r} \times \mathrm{d}\mathbf{r}$, where $\boldsymbol{\mathcal{A}}$ is the area vector associated with the area $\mathcal{A}$ enclosed by the cyclotron orbit. Equation (2.66) now becomes

$$\Phi_n = \frac{2\pi\hbar}{e}\left(n + \frac{1}{2}\right). \tag{2.72}$$

The magnetic flux is quantized, and in a constant field B the area $\mathcal{A}_n$ enclosed by the orbit is also quantized. The quantized areas in real space are

$$\mathcal{A}_n = \frac{2\pi\hbar}{eB}\left(n + \frac{1}{2}\right) = 2\pi\ell_B^2\left(n + \frac{1}{2}\right), \tag{2.73}$$

yielding the quantized radii

$$r_n = \sqrt{\frac{2\hbar}{eB}\left(n + \frac{1}{2}\right)} = \ell_B\sqrt{2n+1} \tag{2.74}$$

where we have defined the magnetic length $\ell_B \equiv \sqrt{\hbar/eB}$. The length r_n in real space is related to the length k_n in reciprocal space by the relation $k_n = r_n/\ell_B^2$, which yields

$$k_n = \sqrt{\frac{2eB}{\hbar}\left(n + \frac{1}{2}\right)} = \frac{\sqrt{2n+1}}{\ell_B}\,. \tag{2.75}$$

If we let $\mathbf{B} = B\hat{\mathbf{z}}$, then the vector potential in the symmetric gauge is $\mathbf{A} = (B/2)\,[-y\hat{\mathbf{x}} + x\hat{\mathbf{y}}]$. Motion in the z-direction is unaffected by the magnetic field, and cyclotron motion is induced in the directions perpendicular to z. This allows us to write the Hamiltonian as a sum of a transverse Hamiltonian and a longitudinal Hamiltonian, given as

$$\mathcal{H} = \mathcal{H}_\perp + \mathcal{H}_z = \frac{1}{2m_e}p_\perp^2 + \frac{1}{2m_e}p_z^2 = \frac{1}{2m_e}\left(p_x^2 + p_y^2\right) + \frac{1}{2m_e}p_z^2\,. \tag{2.76}$$

The transverse Hamiltonian consists of a sum of squares, so we can define the associated creation/annihilation operators by [21]

$$a = \frac{p_y + ip_x}{\sqrt{2\hbar eB}} \qquad \text{and} \qquad a^\dagger = \frac{p_y - ip_x}{\sqrt{2\hbar eB}}\,. \tag{2.77}$$

The transverse Hamiltonian then becomes

$$\mathcal{H}_\perp = \frac{\hbar eB}{m_e}\left(a^\dagger a + \frac{1}{2}\right) = \hbar\omega_c\left(a^\dagger a + \frac{1}{2}\right), \tag{2.78}$$

where we have defined the cyclotron frequency as

$$\omega_c = \frac{eB}{m_e}\,. \tag{2.79}$$

The full Hamiltonian from Eq. (2.76) is therefore

$$\mathcal{H} = \hbar\omega_c\left(a^\dagger a + \frac{1}{2}\right) + \frac{1}{2m_e}p_z^2\,. \tag{2.80}$$

The corresponding eigenenergies are referred to as Landau levels and are given by

$$E_n = E_\perp + E_z = \hbar\omega_c\left(n + \frac{1}{2}\right) + \frac{\hbar^2 k_z^2}{2m_e}\,. \tag{2.81}$$

Equating the transverse energy $E_\perp = \hbar\omega_c(n+1/2)$ with $(\hbar k_\perp)^2/2m_e$ and solving for $k_\perp$, we obtain $k_\perp = k_n = \sqrt{2n+1}/\ell_B^2$ which is the same result that we found in Eq. (2.75).

2.8 The de Haas-van Alphen Effect

The de Haas-van Alphen effect is characterized by oscillations in the magnetization (i.e. the magnetic susceptibility) of a material due to oscillations in the energy caused by Landau quantization.

Consider a free electron undergoing quantized cyclotron motion as in Section 2.7. Given Eq. (2.75), then we can write the area S_n of the orbit in reciprocal space as [11]

$$S_n = \pi k_n^2 = \frac{2\pi}{\ell_B^2}\left(n + \frac{1}{2}\right) = \frac{2\pi eB}{\hbar}\left(n + \frac{1}{2}\right). \tag{2.82}$$

We can can modify our notation slightly by transferring the index n from S to B, which allows us to write

$$\frac{1}{B_n} = \frac{2\pi e}{\hbar S}\left(n + \frac{1}{2}\right). \tag{2.83}$$

Subtracting consecutive indices of Eq. (2.83), we obtain the desired B^{-1} periodicity that characterizes the de Haas-van Alphen effect [11]:

$$\Delta\left(\frac{1}{B}\right) = \frac{1}{B_{n+1}} - \frac{1}{B_n} = \frac{2\pi e}{\hbar S}. \tag{2.84}$$

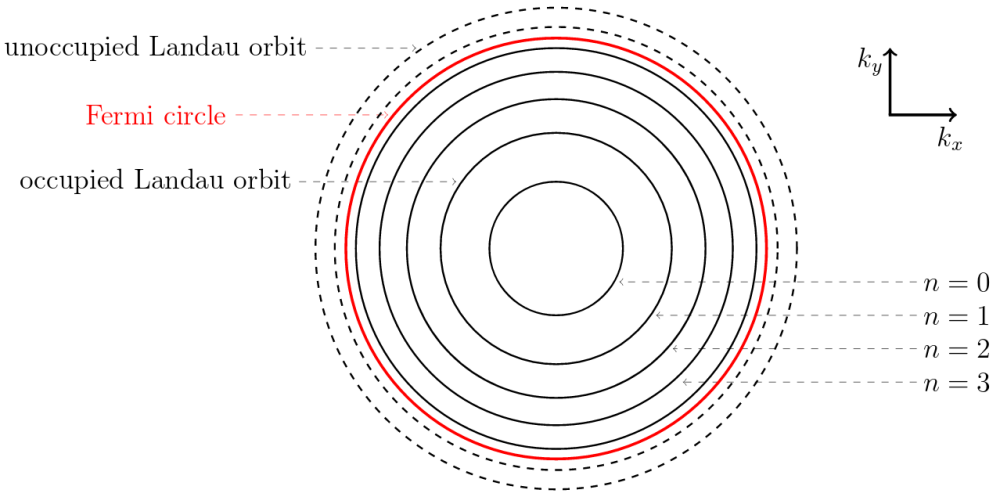

FIGURE 2.7: Projection of the intersections of Landau tubes with the Fermi sphere into the k_x-k_y plane.

The associated frequency is therefore [21]

$$f = \frac{\hbar S}{2\pi e}\,, \tag{2.85}$$

where S here is the extremal area. The extremal area is defined in the context of three dimensional reciprocal space as the cross section of the Fermi sphere perpendicular to the applied field where the cyclotron frequency is approximately constant, i.e. the circular area of radius k_F. Non-extremal cross sections do not produce a net contribution due to phase cancellation.

The number of electrons per Landau level is known as the Landau level degeneracy D. This can be calculated as the difference of circular areas in reciprocal space

$$\Delta S = S_{n+1} - S_n = 2\pi/\ell_B^2\,, \tag{2.86}$$

divided by the area in reciprocal space occupied by a single orbital $(2\pi)^2/\mathcal{A}$. The Landau level degeneracy is therefore

$$D = \frac{\mathcal{A}}{(2\pi)^2}\Delta S = \frac{\mathcal{A}}{2\pi\ell_B^2} = \frac{\mathcal{A}}{2\pi}\frac{eB}{\hbar}\,. \tag{2.87}$$

The number of fully filled Landau levels is therefore

$$s = \text{floor}\left(\frac{N}{D}\right) - 1. \tag{2.88}$$

The total energy of the system can be written as the sum

$$E = E_{\text{filled}} + E_{\text{partial}}\,, \tag{2.89}$$

where

$$E_{\text{filled}} = \sum_{n=0}^{s} D\hbar\omega_c\left(n + \frac{1}{2}\right) \tag{2.90}$$

is the contribution to the energy from the electrons in the fully filled levels and

$$E_{\text{partial}} = \hbar\omega_c\left(s + \frac{3}{2}\right)(N - (s+1)D) \tag{2.91}$$

is the contribution to the energy from the electrons in the partially filled level. The total energy can then be written explicitly as

$$E = \hbar\omega_c \left[N\text{floor}\left(\frac{N}{D}\right) + \frac{N}{2} - \frac{D}{2}\left(\text{floor}\left(\frac{N}{D}\right)\right)^2 - \frac{D}{2}\text{floor}\left(\frac{N}{D}\right)\right]. \tag{2.92}$$

The magnetization of the sample is calculated as $M = -\frac{1}{V}\frac{\partial E}{\partial B}$. Given the magnetization, the magnetic susceptibility can then be calculated as

$$\chi = \frac{\partial M}{\partial H}. \tag{2.93}$$

De Haas-van Alphen oscillations are only visible at low temperatures since as the temperature raises the Landau orbits become "smeared out" and the amplitude of the dHvA oscillations decreases exponentially.

The theory behind the de Haas-van Alphen effect in graphene has been studied extensively [22, 23]. The energy in this case is [24]

$$E_n = \hbar\omega_c\sqrt{n}. \tag{2.94}$$

In contrast to the previous case, there is a state in graphene (namely $n = 0$) in which $E = 0$. The effective mass is given by [25]

$$m^* = \frac{\hbar k}{v_F} = \sqrt{\hbar} v_F \sqrt{\frac{S}{\pi}}. \tag{2.95}$$

The associated cyclotron frequency is

$$\omega_c = v_F\sqrt{\frac{2eB}{\hbar}}. \tag{2.96}$$

The area of the n^{th} orbit in reciprocal space is given by

$$S_n = g_s g_v \frac{2\pi eB}{\hbar} n, \tag{2.97}$$

where $g_s = 2$ accounts for spin degeneracy and $g_v = 2$ accounts for valley degeneracy. Similar to the previous calculation, we can calculate the Landau level degeneracy by

dividing by $(2\pi)^2/\mathcal{A}$ as

$$D = g_s g_v \frac{eB\mathcal{A}}{2\pi\hbar} \,. \tag{2.98}$$

Therefore the dHvA period for graphene is given by

$$\Delta\left(\frac{1}{B}\right) = g_s g_v \frac{2\pi e}{\hbar S} = \frac{8\pi e}{\hbar S} \,. \tag{2.99}$$

Chapter 3

Experimental Setup

The experimental setup of the room temperature magnetometer is based on two fundamental parts, the probe and the electromagnet. The probe (see FIG. 3.1 and FIG. 3.2) is essentially a device which holds the cantilever such that the tip is aligned with the end of a fiber optic cable (see FIG. 3.3) which can be sealed and put under a vacuum within a large electromagnet. The purpose of the electromagnet as simply to provide a uniform magnetic field in the vicinity of the cantilever which can be easily increased/decreased or rotated as the cantilever is held fixed in the lab frame. The laser point is focused on the broad tip of the cantilever, off of which it reflects creating an approximately sinusoidal wave as the cantilever oscillates. The laser also reflects off of the end of the end of the fiber optic cable due to the the difference in refractive indices of the cable and the vacuum. The two optical waves interfere and are converted into voltage waves, allowing the frequency of the cantilever to be measured. When the natural frequency of oscillation of the cantilever is obtained, the cantilever can then be driven at this frequency with a piezo disk.

When a steady vacuum is achieved and the cantilever is being driven at the resonant frequency, the magnetic field is swept between the values $+7000\,\mathrm{G}$ to $-7000\,\mathrm{G}$ in regular intervals, measuring the value of the frequency at each iteration. These frequency values are then used to calculate the magnetic susceptibility given the result in Section 2.5. The setup of the low temperature probe (the ENDOR probe) is similar in the way that it uses interferometry to detect the frequency of the cantilever, but is necessarily more complicated in order to withstand the rapid freezing and thawing process involved with

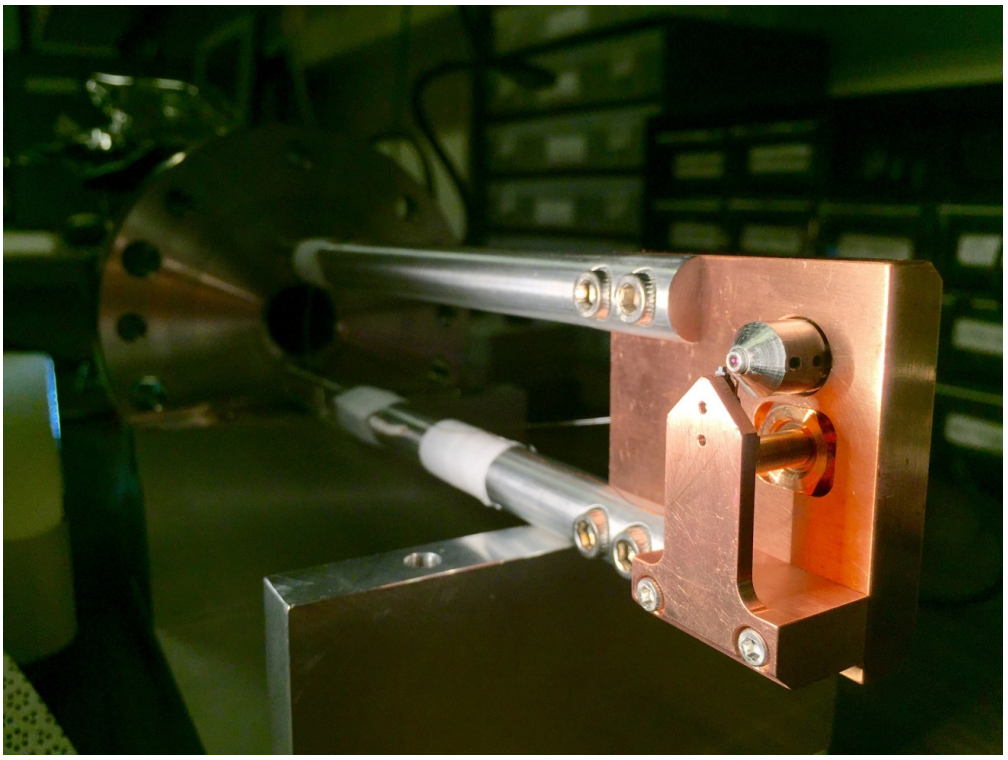

FIGURE 3.1: Probe used to perform cantilever magnetometry at room temperature.

liquid Nitrogen and liquid Helium. A superconducting coil is used when cooled to 4 K allowing for a much more powerful magnetic field (up to 5 T). The probe and the coil are placed into a dewer which is eventually chilled to 4 K with liquid Helium. The space within the sealed probe is evacuated of air, and measurements of the frequency are made as the magnetic field is varied. The relative orientations of the cantilever and the magnetic field are not easily varied using the ENDOR probe, and measurements are significantly more costly, so use of this probe is limited to only the more pristine samples.

Care was taken to construct the elements of the probe with materials that are weakly magnetic, e.g. brass and copper. FIG. 3.3 shows the process of alignment of the cantilever with the optical laser. The laser appears as a white dot which in this figure is not currently in-between the two center ultrasoft cantilevers, of which there are six. As shown in FIG. 4.5, the ultrasoft cantilevers used in this study have a length of 120 μm.

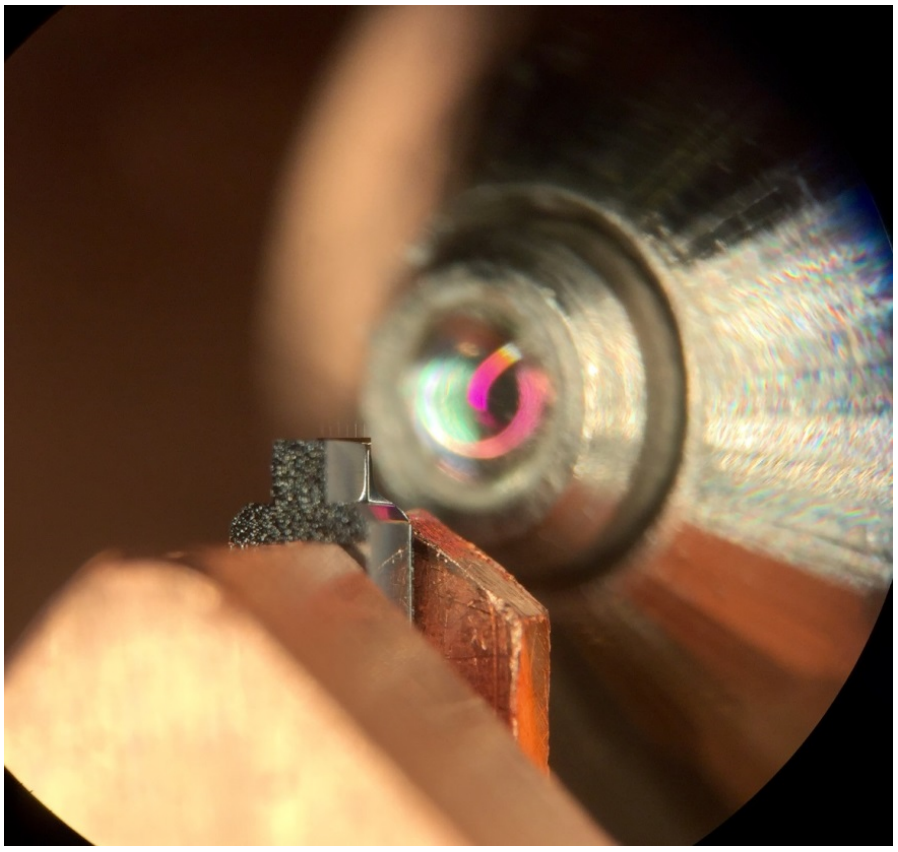

FIGURE 3.2: Zoomed-in image of cantilever and bullet.

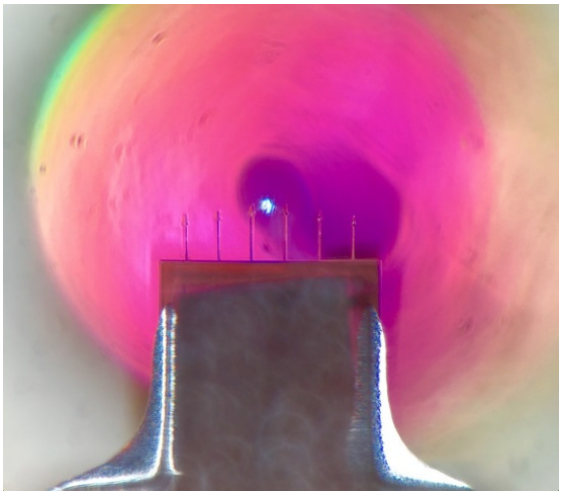

FIGURE 3.3: Close-up of the cantilever and optical laser as viewed down the axis of symmetry of the bullet.

Chapter 4

Sample Preparation

The process of sample preparation detailed in this chapter constitutes the majority of the challenge with respect to obtaining the measurements presented in Chapter 5. The fundamental quandary is this: how can one transfer a delicate two-dimensional material onto a delicate cantilever without compromising the integrity of either? The solution was developed by N. Scozzaro and S. Singh [17], and involves pressing ("stamping") the tip of the cantilever firmly onto a substrate containing exfoliated graphene.

Two stamping methods have been employed, each with their associated advantages and drawbacks. The first method is to exfoliate graphene directly onto a dry PDMS substrate. In order to press the tip of the cantilever against the substrate, there must necessarily be a surface behind the cantilever with which to press against or the cantilever will not survive the process. In order to solve this problem, the tip of the cantilever is rested on a neighboring cantilever chip as shown in FIG. 4.1 and glued down with G1. The equipment used to press the cantilever platform against the inverted PDMS substrate is known as the transfer tool and is shown in FIG. 4.2.

The second method is to obtain a substrate comprised of silicon, on top of which contains a thin layer of polyacrylic acid, that has been spin-coated onto the surface. When dry, a layer of PMMA is spin-coated onto the polyacrylic acid such that the substrate appears pink/purple when viewed directly. An example of such substrates are shown in FIG. 4.3. Graphene exfoliated with basic household tape is pressed onto the PMMA-coated substrates. The substrates are floated on the surface of distilled water, causing the polyacrylic layer to dissolve. The graphene and PMMA therefore separate

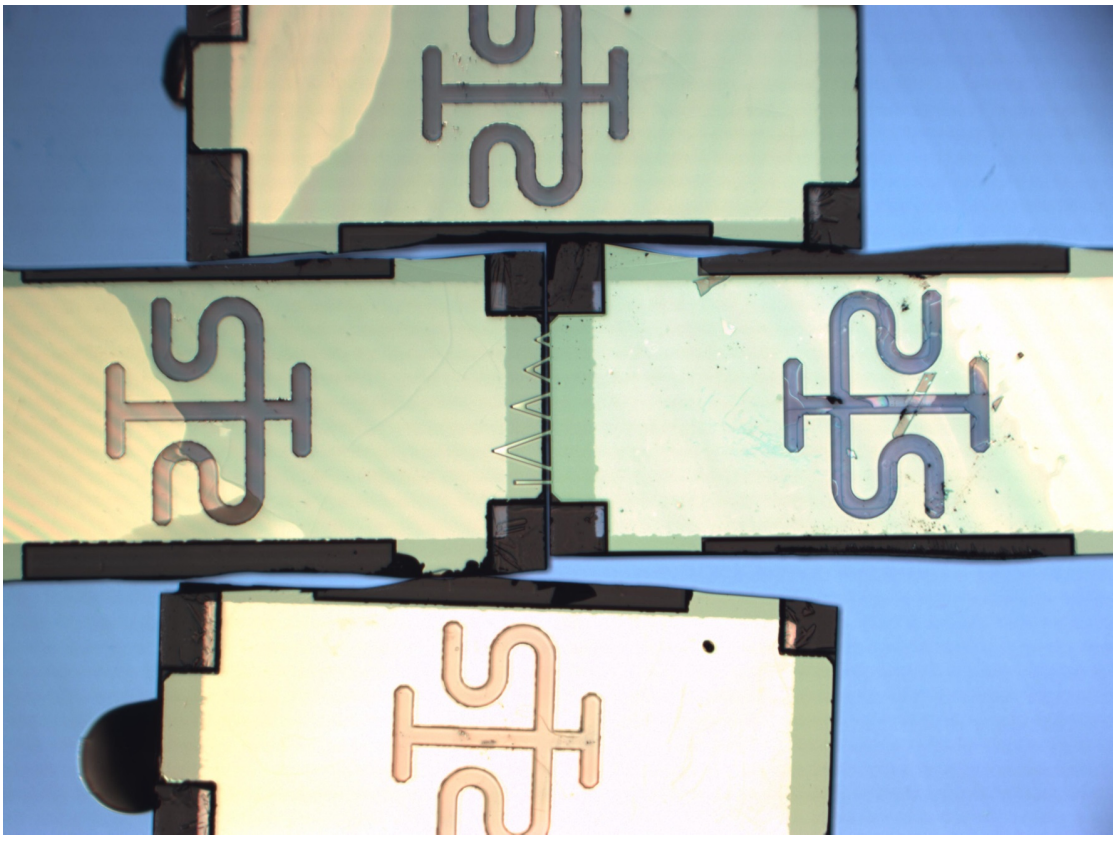

FIGURE 4.1: Cantilever platform used to stamp graphene onto cantilever.

from the silicon substrate as it floats on the surface. Once separation is complete, the PMMA is scooped up onto a PDMS substrate. From this point the rest of the process is the same as for the first method, except that during stamping the PMMA must be melted off of the PDMS at 150 degrees celsius. As such, the transfer tool is equipped with a heating element.

The advantages to the dry PDMS method is that the recovered cantilever is not covered in polymer, but as a result the graphene is difficult to become unstuck to the PDMS, making it difficult more difficult to transfer. The advantage to the PMMA method is that there is a higher probability of performing a successful transfer, but the drawback is that the cantilever is now covered in polymer which must be cleaned or risk destroying the quality factor of the cantilever.

The transfer tool can be used repeatedly to obtain stacks of monolayer graphene encapsulated by other monolayers (or multilayers). This allow a hBN-graphene-hBN stack to be created, as shown in FIG. 4.4.

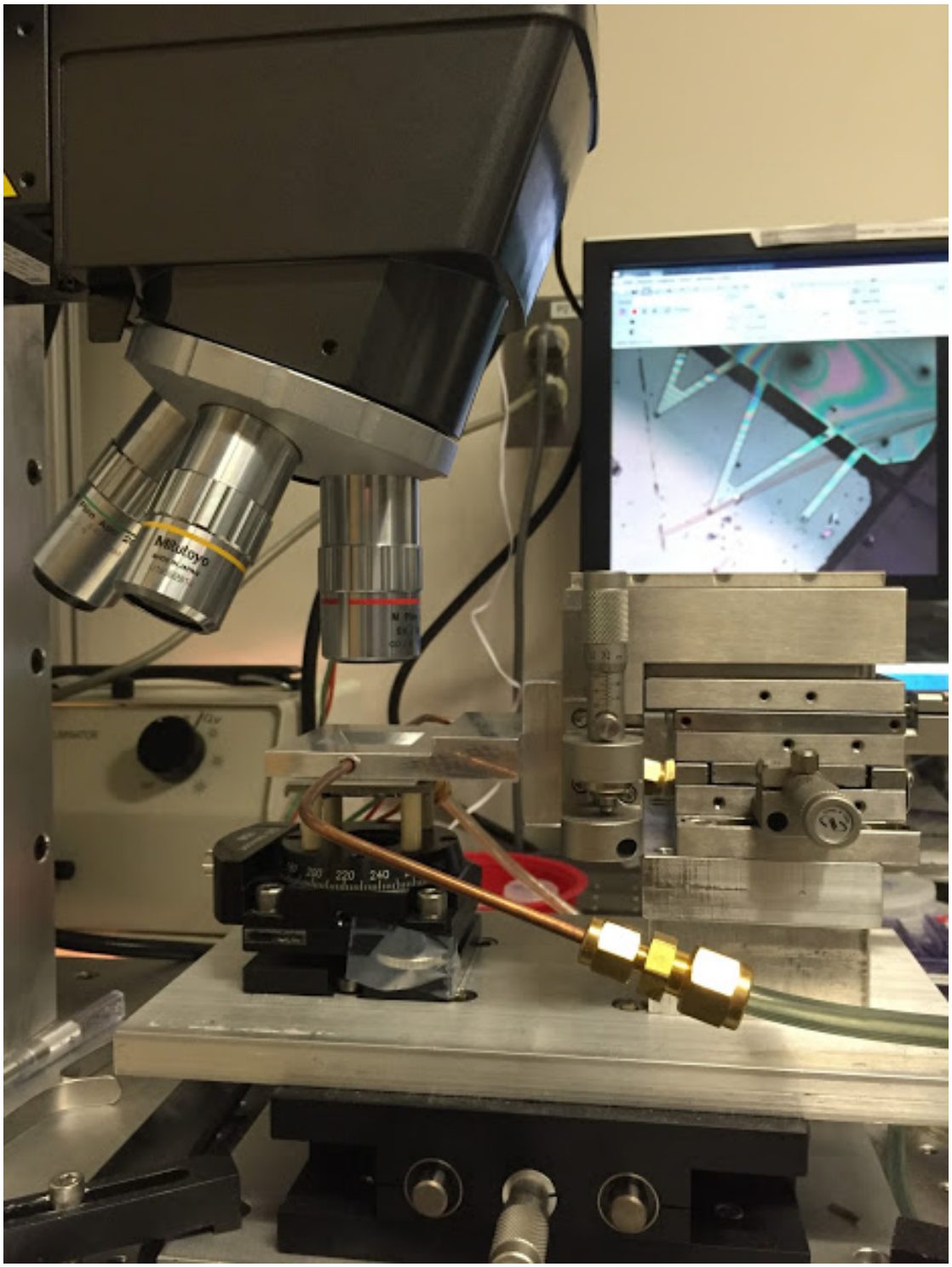

FIGURE 4.2: Transfer tool used to stamp graphene onto cantilever.

Cantilevers come in various shapes and sizes. The two types of cantilevers used here are triangle cantilevers (see FIG. 4.4) and ultrasoft cantilevers (see FIG. 4.5). For this experiment it is essential to use a cantilever soft enough to have a reasonable signal to noise ratio, but strong enough to survive the stamping process without significant

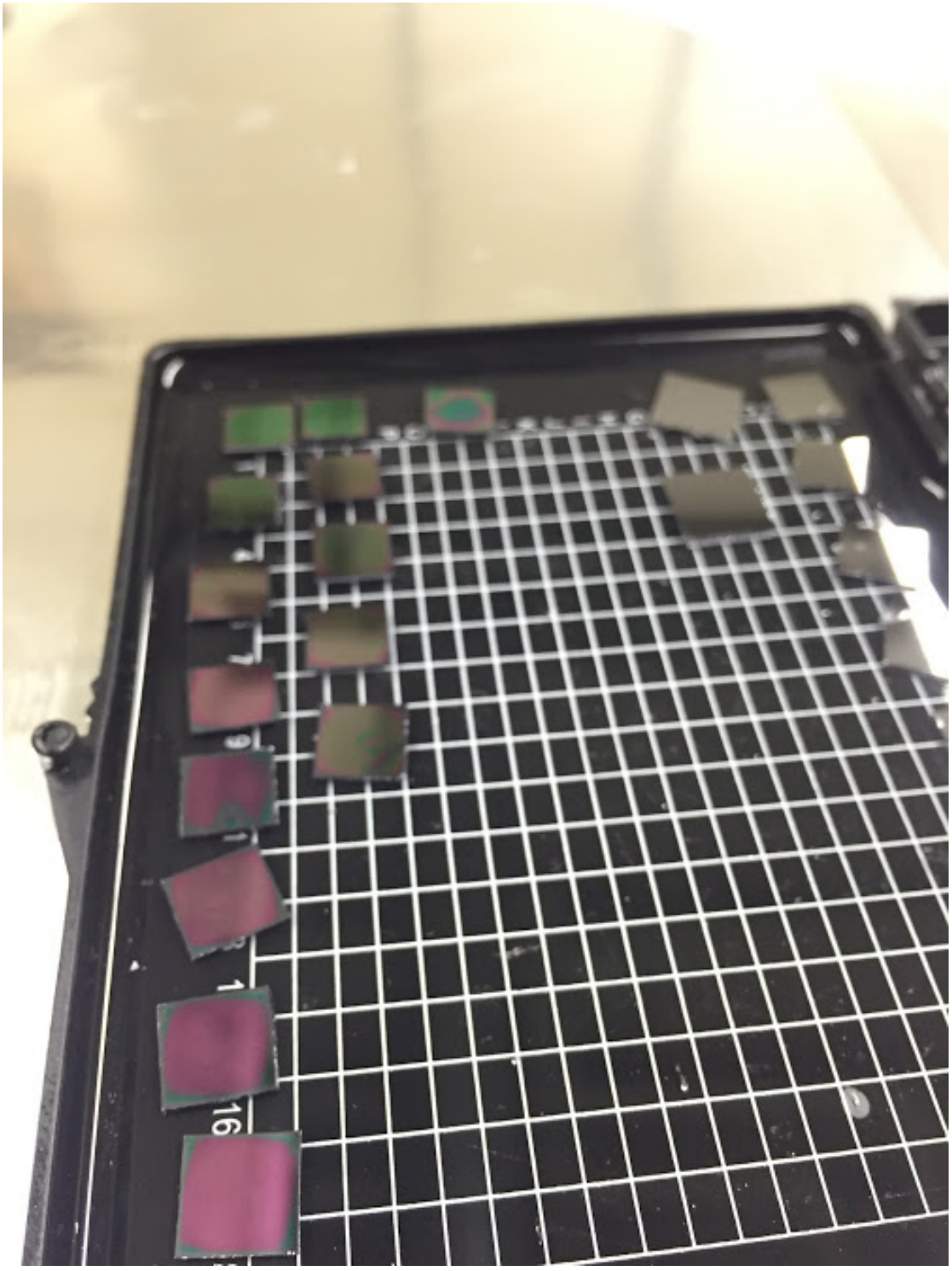

FIGURE 4.3: Silicon substrates containing spin-coated layers of polyacrylic acid and PMMA with characteristic pink color (bottom left).

distortion. The cantilevers used in this study would make very poor AFM cantilevers due to their softness.

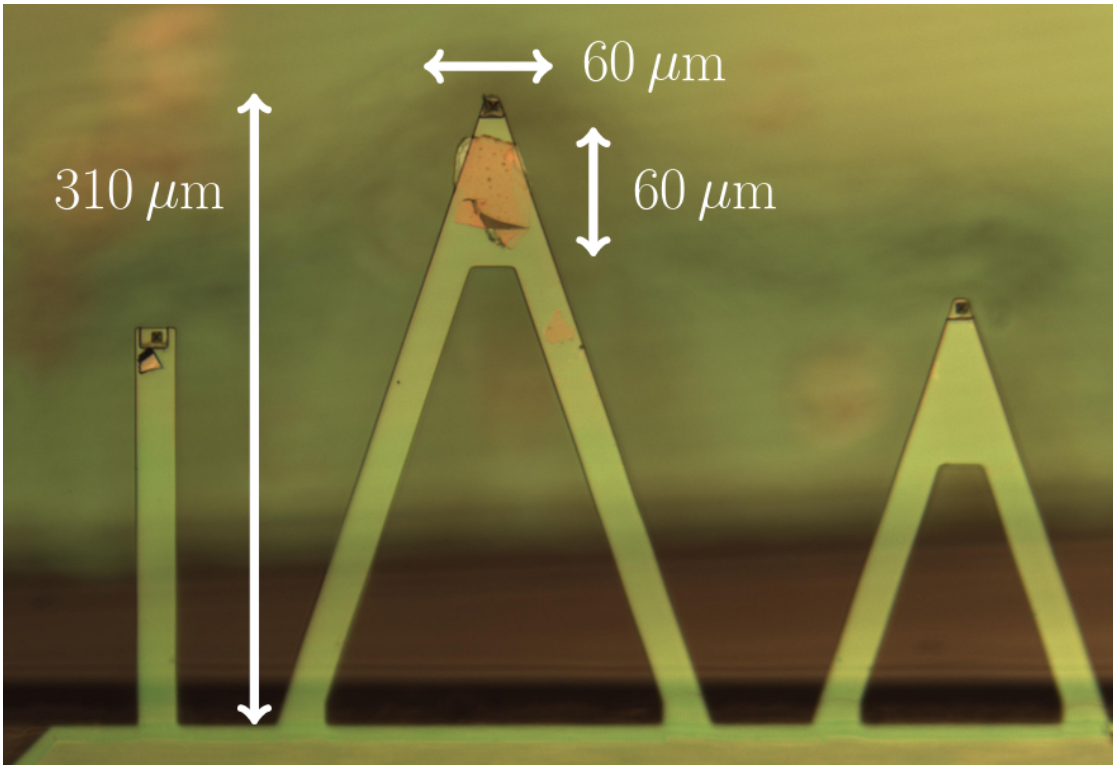

FIGURE 4.4: Triangle cantilever with graphene double encapsulated in hexagonal boron nitride.

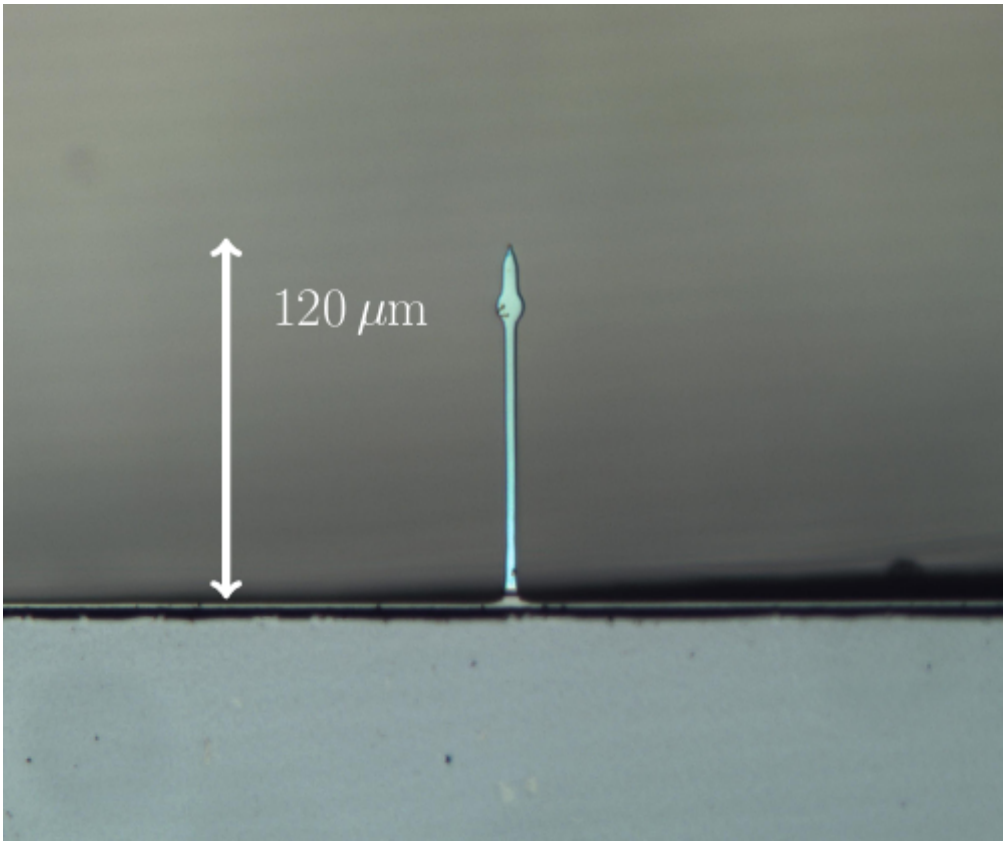

FIGURE 4.5: Triangle cantilever with graphene double encapsulated in hexagonal boron nitride.

Chapter 5

Results & Discussion

In this chapter the results obtained are presented and discussed. We begin each section by detailing control tests that have been made, i.e. magnetometry data taken with cantilevers that do not contain a sample. This has allowed us to characterize our cantilevers, yielding a reference by which to compare our experimental results. Section 5.1 presents the data taken at room temperature (∼300 K) on both triangle cantilevers and ultrasoft cantilevers. The final section provides the data taken at low temperature (∼4 K) as well as control tests taken at low temperature.

5.1 Measurements at Room Temperature

At room temperature a bare cantilever is expected to not have a measurable response as the magnetic field is applied for various strengths and angles. Indeed, this is what we have observed with a level of noise on the order of 10 mHz, although this noise level can vary dramatically from cantilever to cantilever. The typical frequency a cantilever falls in the range of 5-8 kHz, with a quality factor of about 10,000-20,000.

In Section 2.5 we calculated the expected frequency shift for a magnetic field of a given magnitude and orientation, finding it to be approximately directly proportional to the magnetic susceptibility. The dependence of the frequency shift on the magnitude of the magnetic field is quadratic and is proportional to $\cos(2\theta)$ where θ represents the angle between the magnetic field and the equilibrium position of the cantilever. At room temperature these measurements where performed with a triangle cantilever containing

a ∼300-layer graphite flake as shown in FIG. 5.1. Indeed, we observe the expected parabolas with the expected phase factor.

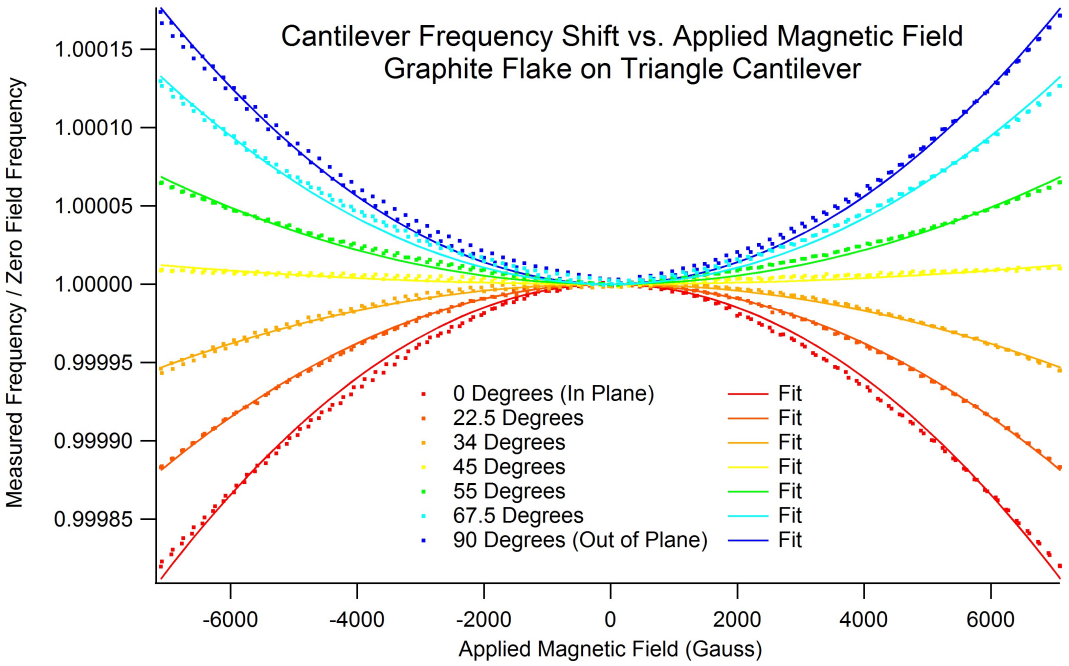

FIGURE 5.1: Room temperature measurement of frequency shift vs. applied magnetic field of 300-layer graphite flake on triangle cantilever.

We successfully created a cantilever estimated to contain a sample of six-layer graphene using an ultrasoft cantilever in this case instead of a triangle cantilever. Room temperature magnetometry was performed and the results for the frequency shift vs. field are shown in FIG. 5.2. As can be seen, the relative noise level for the 6-layer graphene is noticeably higher than for the 300-layer sample. This is most likely due to the significantly weaker force on the cantilever tip since 6-layer graphene will produce a weaker induced field than 300-layer graphite.

In FIG. 5.3 are the data taken of the (unnormalized) frequency of the cantilever as a function of the external field for a ∼3-layer sample of graphene. The cantilever used in this trial was also an ultrasoft cantilever. In this figure magnetometry has only been done in two orientations, and the noise level is clearly much higher as we approach the limit of the cantilever's sensitivity. Not all cantilevers have the same signal to noise ratio, and it is essential to use the best possible cantilever for a monolayer graphene in order to observe a signal.

In order to isolate a single sheet of graphene, one can create a "sandwich" where the graphene stacked between two other van der Waals materials. We successfully created a

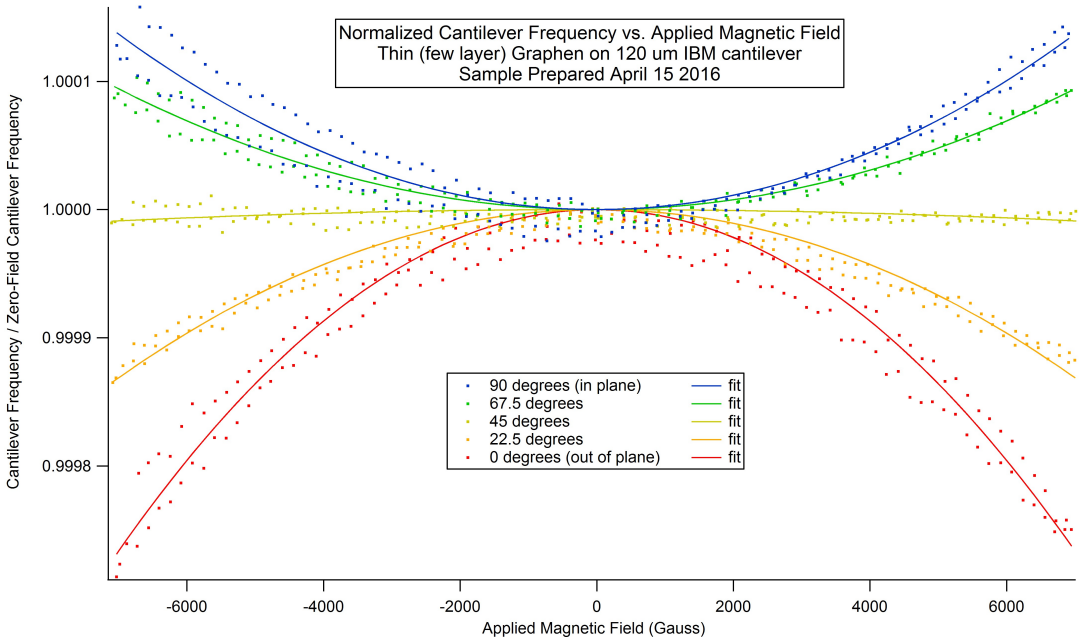

FIGURE 5.2: Room temperature measurement of frequency shift vs. applied magnetic field of ∼6-layer graphene on ultrasoft cantilever.

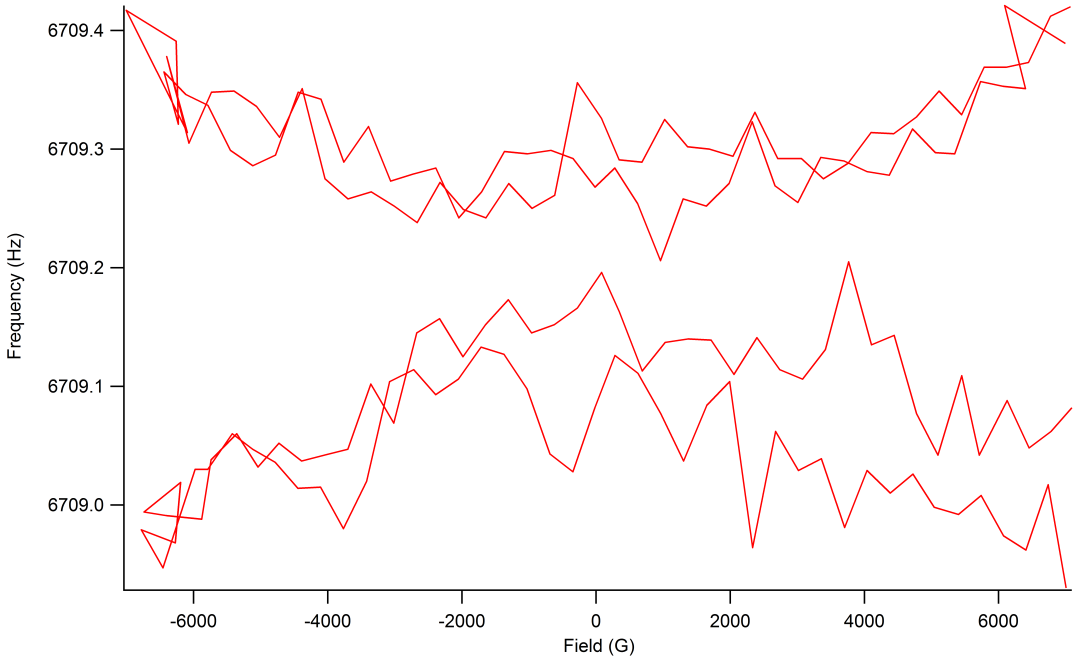

FIGURE 5.3: Room temperature measurement of frequency shift vs. applied magnetic field of ∼ 3-layer graphene on ultrasoft cantilever.

stack in which two comparable sheets of hexagonal boron nitride were used to sandwich monolayer graphene. This stack was deposited on the tip of a triangle cantilever (see FIG. 4.4) and measured at room temperature and at low temperature. After the cooling process the cantilever was measured again at room temperature, yielding unexpected

results. Namely, the signal at room temperature post-cooling was significantly larger than that measured pre-cooling, a phenomenon that we have not been able to reproduce.

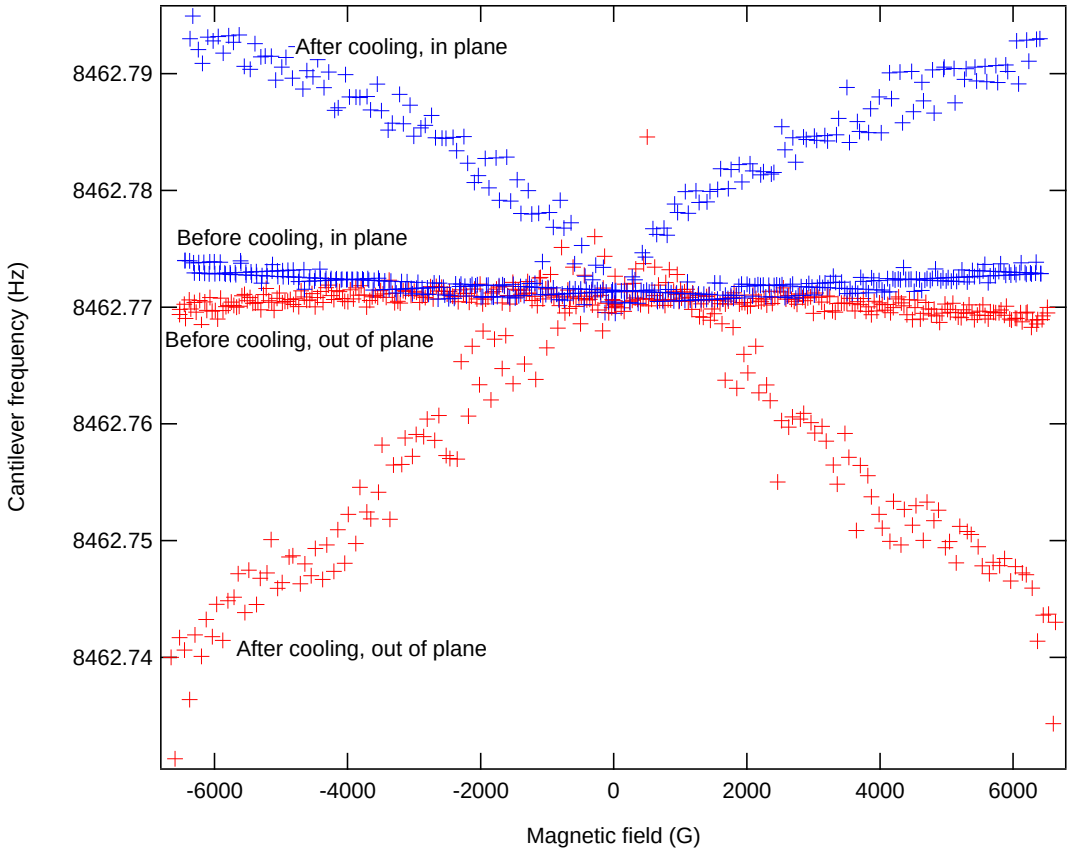

FIGURE 5.4: Graphene encapsulated by hexagonal boron nitride before and after cooling.

5.2 Measurements at Low Temperature

The measurements in this section were performed at low temperature, which in this case is 4 K using liquid Helium. We took data from several control tests at low temperature, i.e. bare cantilevers, and obtained more unexpected activity. In FIG. 5.5 we observe that the quality factor of this particular cantilever plummets as the magnetic field is applied, bottoming out around 2 T but never fully recovering. At low temperature the laser power appears to have a significant effect on the shape of the frequency shift (see FIG. 5.8), and as such two different laser powers were used in FIG. 5.5. From this the associated damping was calculated and plotted in FIG. 5.6 for the same values of laser power. This damping of the low temperature cantilever at high fields is unexpected and highly undesirable for our purposes here. The mechanism behind this phenomenon is left to speculation.

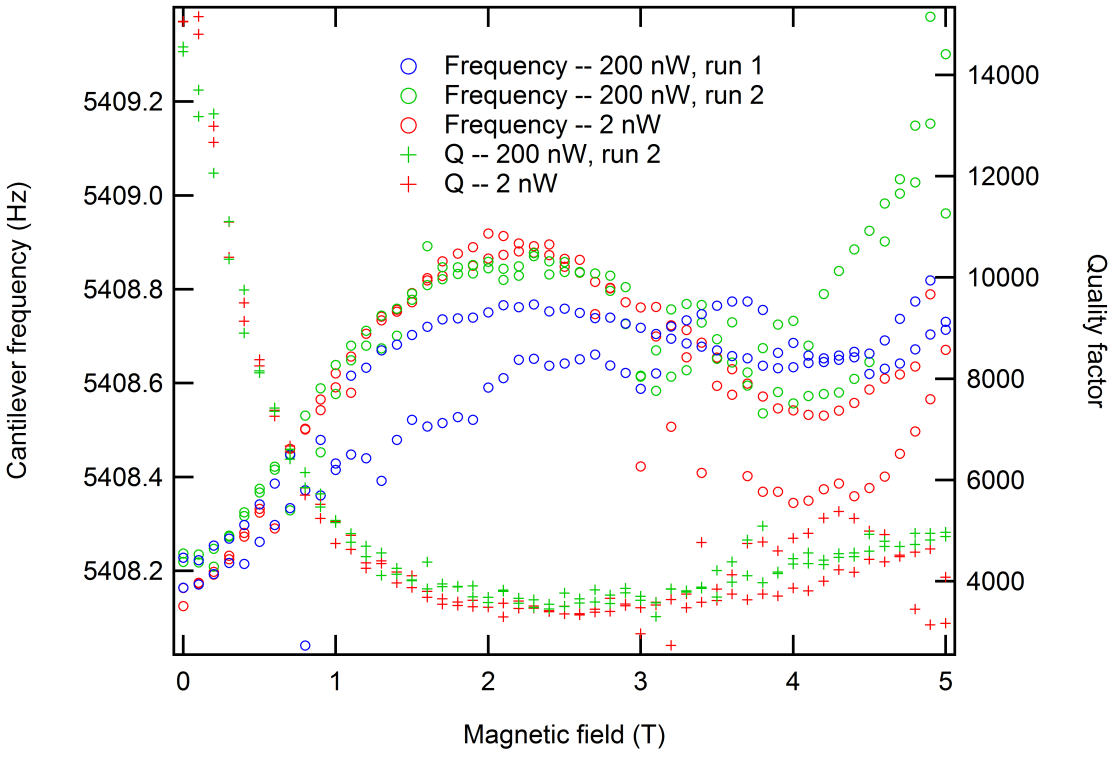

FIGURE 5.5: Frequency and quality factor of bare cantilever plotted as functions of the magnetic field at low temperature.

A sample of hexagonal boron nitride was measured at low temperature, producing the results shown in FIG. 5.7. The signal obtained did not immediately match that of the predicted response, i.e. is not parabolic except for perhaps instantaneously at zero field. However it should be noted that cantilever magnetometry is not limited to

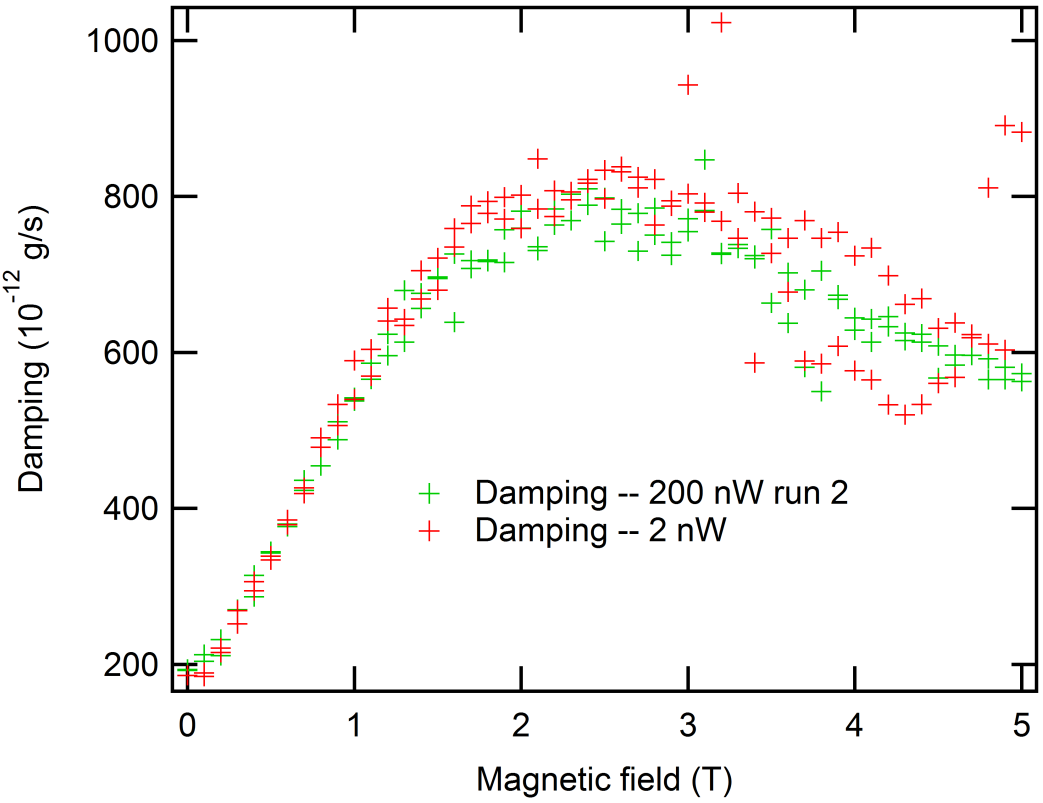

FIGURE 5.6: Damping vs. applied magnetic field at low temperature.

materials such as graphene or even two-dimensional materials, provided one can obtain an analytic expression for the expected frequency shift based on the specific geometry of the object. We also observed the laser itself driving the cantilever's oscillation at 4 K, most likely caused by uneven heating of the cantilever.

5.3 Measurements of the de Haas-van Alphen period.

Taking measurements at 4 K allows the observation of de Haas-van Alphen oscillations in materials such as graphene or graphite. These oscillations are caused by the fact that itinerant electrons moving in a high magnetic field naturally move in quantized cyclotron orbits due to Landau quantization as shown in Section 2.7 and 2.8. As the relative occupations of the Landau levels changes, the total energy has an oscillatory component proportional to the inverse of the applied magnetic field. Normally at room temperature these oscillations are undetectable given that the temperature associated with the electrons causes neighboring orbits to "smear into each other". However at low temperatures (such as 4 K) these measurements can be performed with success. In

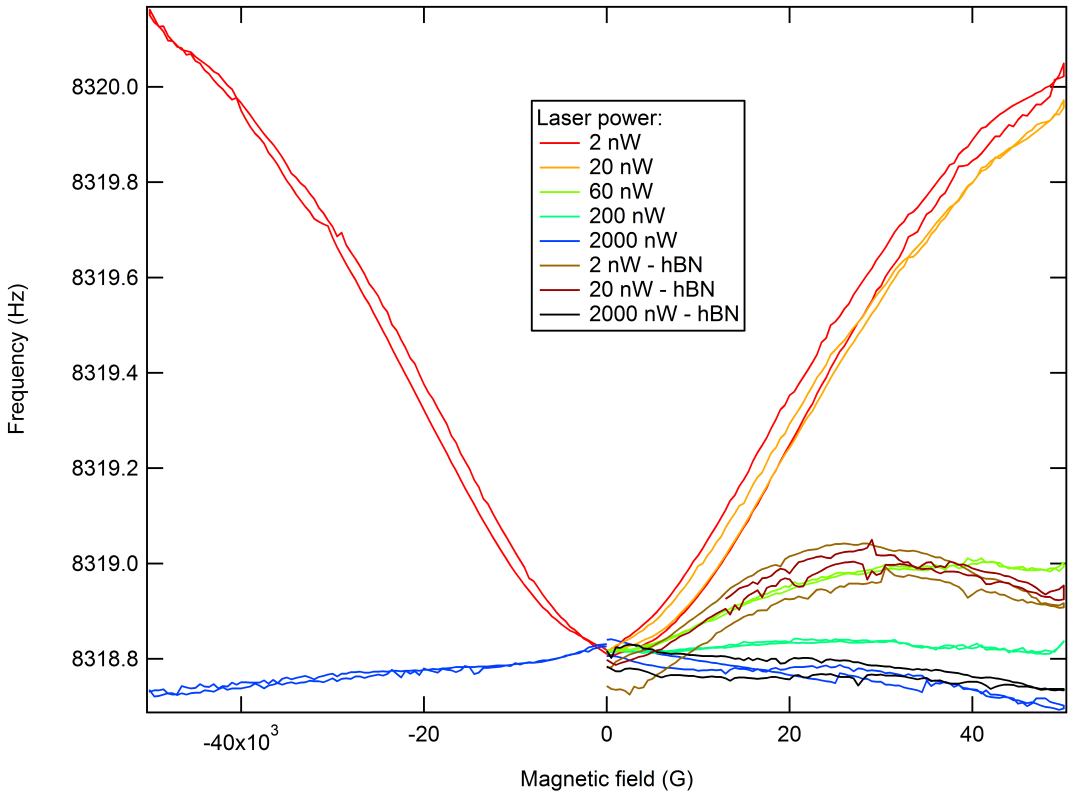

FIGURE 5.7: Frequency vs field for hexagonal boron nitride at low temperature.

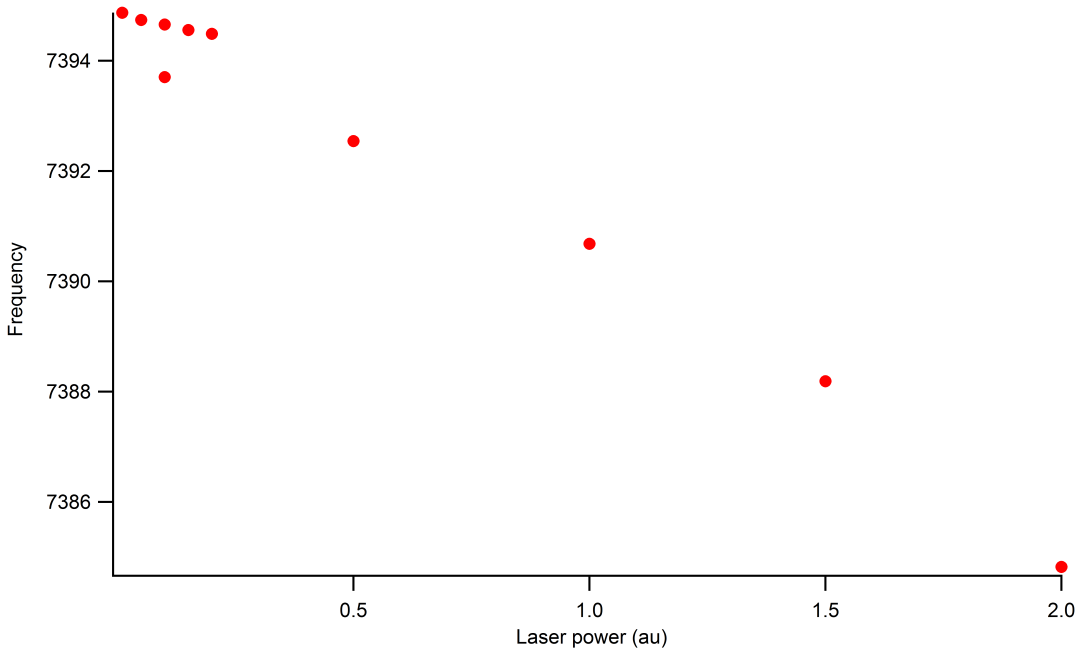

FIGURE 5.8: Cantilever frequency vs power at low temperature for 300-layer graphite flake.

this section we present the data taken at low temperature in which the dHvA can be observed.

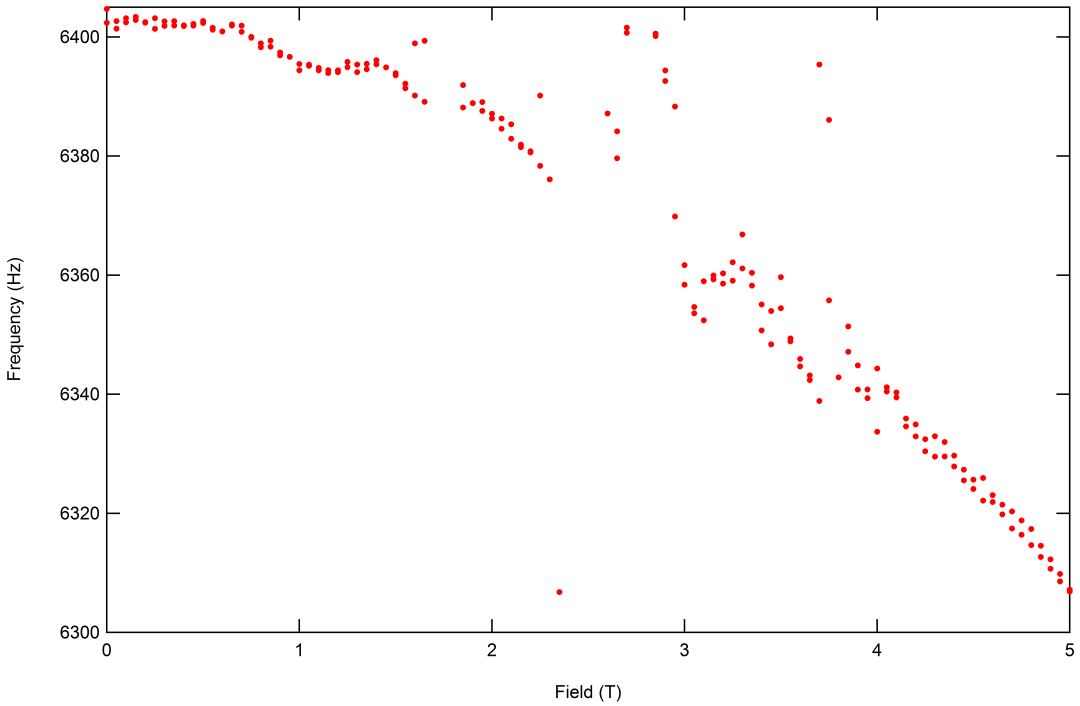

FIGURE 5.9: Cantilever frequency vs field at low Temperature for 6-layer graphene on ultrasoft cantilever.

In FIG. 5.9 data of the cantilever frequency vs the applied field was taken at low temperature with the cantilever containing the 6-layer graphene. It appears that de Haas-van Alphen oscillations were just beginning to manifest when the frequency of the cantilever began to exhibit spurious behavior. Unfortunately we were not able to extract a de Haas-van Alphen period from FIG. 5.9, but it appears that this is possible in principle. It is believed that damage done to the cantilever during the transfer process, causing the cantilever to momentarily jump into a different mode of oscillation, yielding the spurious data.

When magnetometry was performed at low temperature on the 300-layer graphite, we obtained interesting results. The frequency vs. field data is shown in FIG. 5.10 along with the residual, i.e. the leftover signal after the parabolic term is removed. When the the data is plotted versus the inverse of the magnetic field, we obtain the result presented in FIG. 5.11.

The magnetic susceptibility was calculated from the data in FIG. 5.11 (see Section 2.8) and plotted in FIG. 5.12 versus the inverse of the applied field. This yields a period of $\Delta(1/B) = 0.25\,\mathrm{T}^{-1}$.

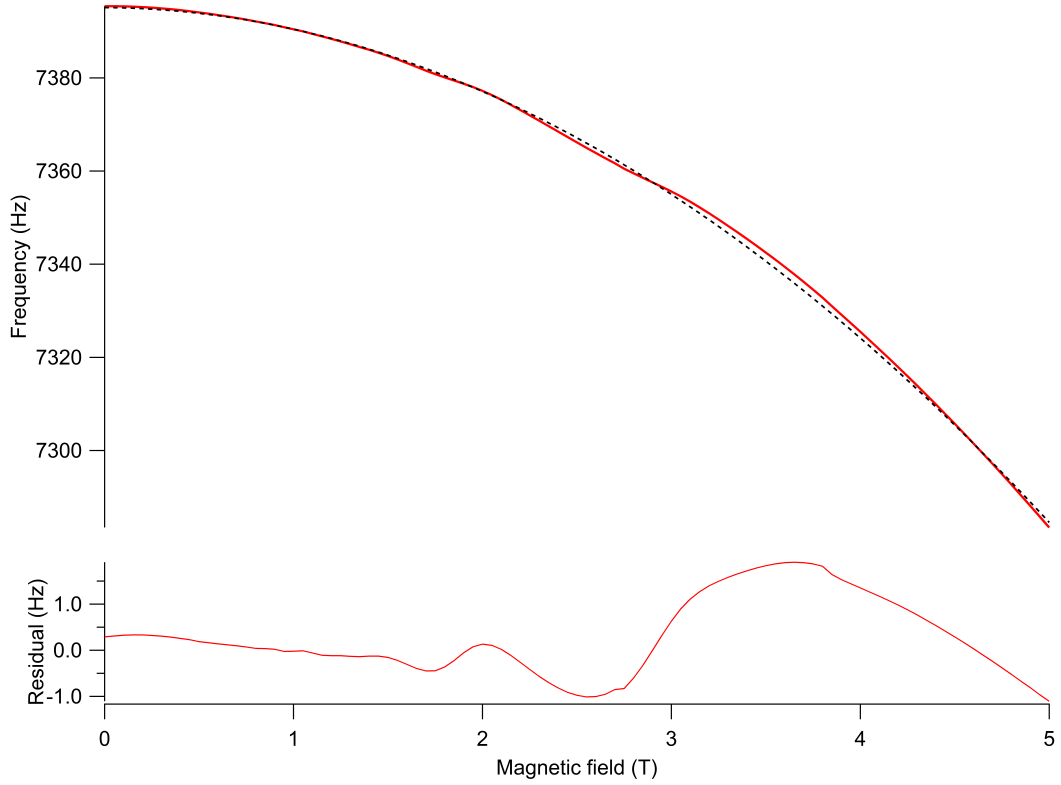

FIGURE 5.10: Frequency vs applied field data and residual for 300-layer graphite at low temperature on triangle cantilever.

The possible directions in which this project could be expanded are multidimensional. As mentioned previously, nothing about the experimental technique of cantilever magnetometry requires the use of graphene or even a two-dimensional material. This opens the possibility of measuring other materials such as hexagonal boron nitride (as we have done here) or molybdenum disulfide. Performing cantilever magnetometry with ferromagnetic samples allows one to also obtain an estimate of the associated anisotropy of the material. Further, this project can be modified a near infinite number of ways (e.g. adding a capacitive element) in order to obtain more detailed information.

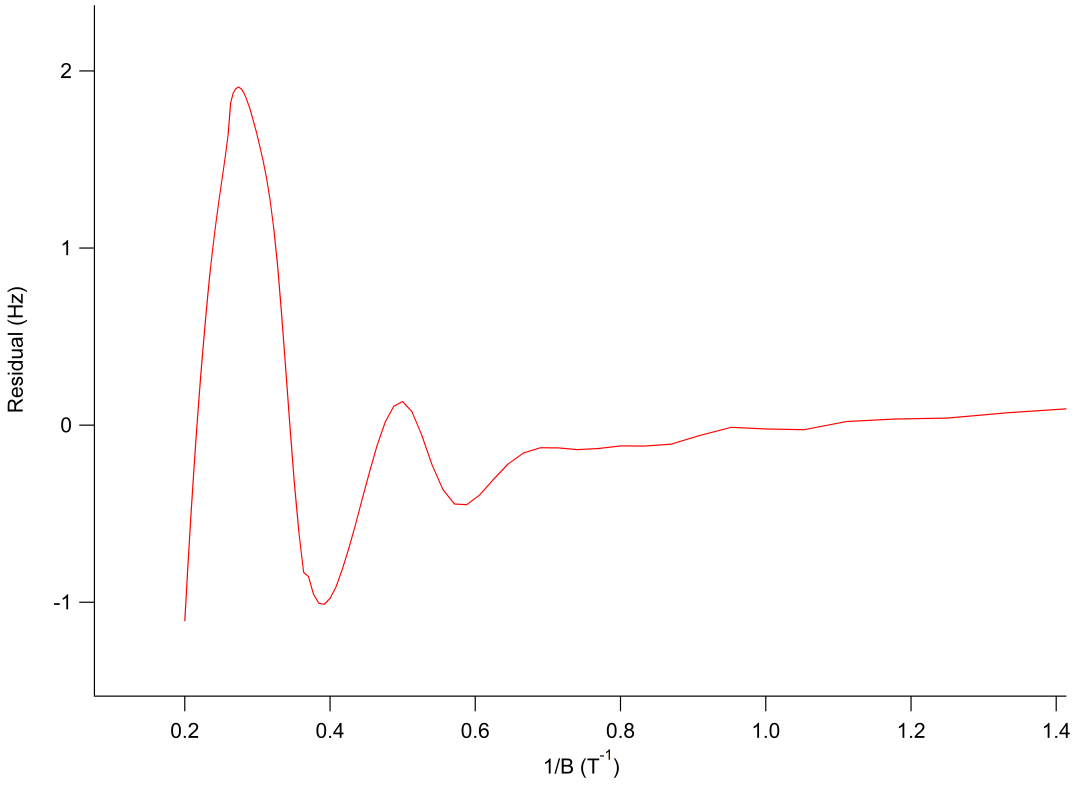

FIGURE 5.11: Frequency residual plotted vs inverse magnetic field for 300-layer graphite at low temperature on triangle cantilever.

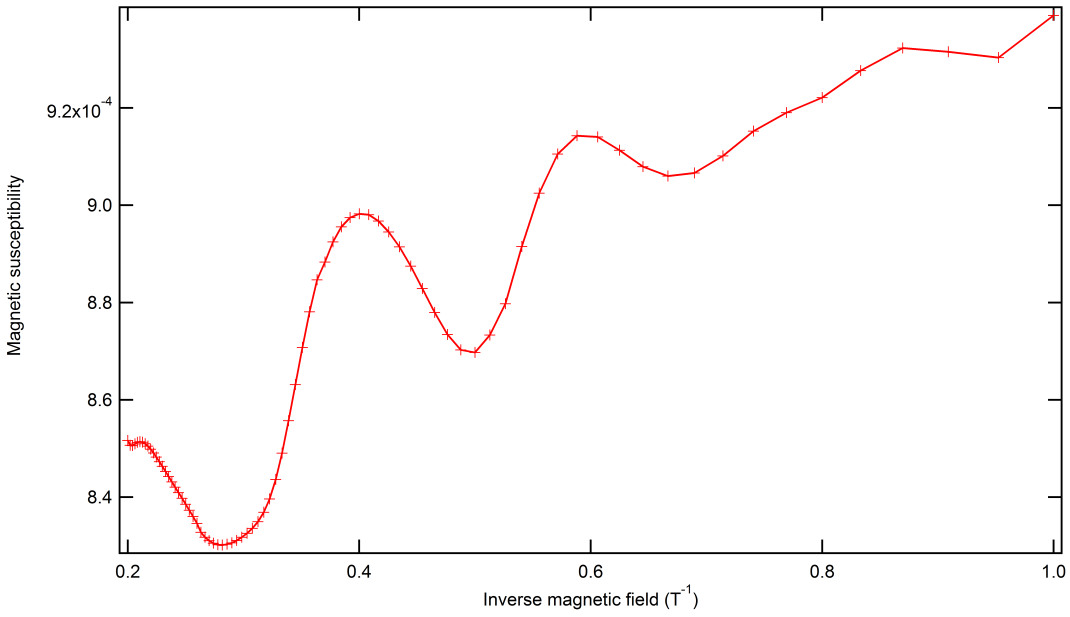

FIGURE 5.12: Magnetic susceptibility vs inverse magnetic field at low temperature for 300-graphite on triangle cantilever.

Bibliography

[1] P. R. Wallace. The band structure of graphite. *Phys. Rev.*, 71:622–634, (1947). URL https://doi.org/10.1103/PhysRev.71.622.

[2] A. K. Geim and K. S. Novoselov. The rise of graphene. *Nature Materials*, 6:183–191, (2007). URL http://dx.doi.org/10.1038/nmat1849.

[3] K. S. Novoselov, A. K. Geim, S. V. Morozov, D. Jiang, Y. Zhang, S. V. Dubonos, I. V. Grigorieva, and A. A. Firsov. Electric field effect in atomically thin carbon films. *Science*, 306:666–669, (2004). URL https://arxiv.org/abs/cond-mat/0410550.

[4] J. H. Chen, C. Jang, M. Ishigami, S. Xiao, E. D. Williams, and M. S. Fuhrer. Diffusive charge transport in graphene on sio_2. *Solid State Communications*, 149: 1080, (2009). URL https://arxiv.org/abs/0812.2504.

[5] J. H. Chen, C. Jang, S. Xiao, M. Ishigami, and M. S. Fuhrer. Intrinsic and extrinsic performance limits of graphene devices on sio_2. *Nature Nanotechnology*, 3:206–209, (2008). URL http://dx.doi.org/10.1038/nnano.2008.58.

[6] A. Akturk and N. Goldsman. Electron transport and full-band electron-phonon interactions in graphene. *Journal of Applied Physics*, 103:053702, (2008). URL http://aip.scitation.org/doi/10.1063/1.2890147.

[7] R. Weast. *Handbook of Chemistry and Physics*. Chemical Rubber Company Publishing, (1975). ISBN 0-8493-0464-4.

[8] A. H. Castro Neto, F. Guinea, N. M. R. Peres, K. S. Novoselov, and A. K. Geim. The electronic properties of graphene. *Rev. Mod. Phys.*, 81:109, (2009). URL https://arxiv.org/abs/0709.1163.

[9] H. Lipson and A. R. Stokes. A new structure of carbon. *Nature*, 149:328, (1942). URL http://dx.doi.org/10.1038/149328a0.

[10] S. H. Simon. *The Oxford Solid State Basics.* Oxford University Press, (2016). ISBN 978-0-19-968076-4.

[11] C. Kittel. *Introduction to Solid State.* John Wiley & Sons, (1996). ISBN 978-0471415268.

[12] J. C. Slonczewski and P. R. Weiss. Band structure of graphite. *Phys. Rev. Lett.*, 109:272, (1958). URL https://doi.org/10.1103/PhysRev.109.272.

[13] J. D. Jackson. *Classical Electrodynamics.* John Wiley & Sons, (1998). ISBN 2900471309320.

[14] D. J. Griffiths. *Introduction to Electrodynamics.* Pearson, (2012). ISBN 978-0321856562.

[15] P. Banerjee *et al.* Magnetization reversal in an individual 25 nm iron-filled carbon nanotube. *Applied Physics Letters*, 96:2010, (1942). URL http://scitation.aip.org/content/aip/journal/apl/96/25/10.1063/1.3440951.

[16] B. C. Stipe, H. J. Mamin, T. D. Stowe, T. W. Kenny, and D. Rugar. Magnetic dissipation and fluctuations in individual nanomagnets measured by ultrasensitive cantilever magnetometry. *Phys. Rev. Lett.*, 86:2874–2877, (2001). URL http://link.aps.org/doi/10.1103/PhysRevLett.86.2874.

[17] N. J. Scozzaro. Ultrasensitive measurements of magnetism in carbon-based materials. *Ph.D. thesis, The Ohio State University, Diss.*, (2016).

[18] J. R. Taylor. *Classical Mechanics.* University Science Books, (2005). ISBN 978-1891389221.

[19] J. Heremans, C. H. Olk, and D. T. Morelli. Magnetic susceptibility of carbon structures. *Phys. Rev. B*, 49:15122–15125, (1994). URL http://link.aps.org/doi/10.1103/PhysRevB.49.15122.

[20] J. M. Gere and S. P. Timoshenko. *Mechanics of Materials.* PWS Publishing Company, (1997). ISBN 978-0534951023.

[21] S. G. Albert. Torque magnetometry on graphene and fermi surface properties of vb2 and mnb2 single crystals studied by the de haas-van alphen effect. *Ph.D. thesis, München, Technische Universität München, Diss.*, (2016). URL https://mediatum.ub.tum.de/doc/1241081/1241081.pdf.

[22] I. A. Luk'yanchuk. De haas van alphen effect in 2d systems: Application to mono- and bilayer graphene. *Low Temperature Physics*, 37:45–48, (2011). URL http://scitation.aip.org/content/aip/journal/ltp/37/1/10.1063/1.3551529.

[23] S. G. Sharapov, V. P. Gusynin, and H. Beck. Magnetic oscillations in planar systems with the dirac-like spectrum of quasiparticle excitations. *Phys. Rev. B.*, 69:075104, (2004). URL http://link.aps.org/doi/10.1103/PhysRevB.69.075104.

[24] J. W. McClure. Diamagnetism of graphite. *Phys. Rev.*, 104:666–671, (1956). URL http://link.aps.org/doi/10.1103/PhysRev.104.666.

[25] V. Ariel and A. Natan. Electron effective mass in graphene. *Electromagnetics in Advanced Applications (ICEAA), 2013 International Conference*, pages 696–698, (IEEE, 2013).